

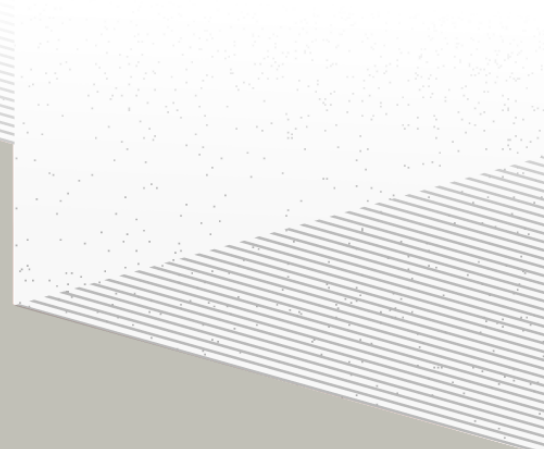
1

2

# THÈSE DE DOCTORAT DE

L'UNIVERSITÉ DE NANTES

ÉCOLE DOCTORALE N°596  
*Matière, Molécules, Matériaux*  
Spécialité : *Physique des particules*



Par

**Léonard Imbert**

**Precision measurement of solar neutrino oscillation parameters  
with the JUNO small PMTs system and test of the unitarity of the  
PMNS matrix**

Thèse présentée et soutenue à Nantes, le Too soon and too early at the same time  
Unité de recherche : Laboratoire SUBATECH, UMR 6457

## Rapporteurs avant soutenance :

Someone	Very high position, Somewhere
Someone else	Another high position, Somewhere else

## Composition du Jury :

Président :	Jacques Chirac	French president, France
Examinateurs :	Yoda	Master, Dagobha
Dir. de thèse :	Frédéric Yermia	Professeur, Université de Nantes
Co-dir. de thèse :	Benoit Viaud	Chargé de recherche, CNRS

## Invité(s) :

Victor Lebrin Docteur, CNRS/SUBATECH



## <sup>3</sup> List of Abbreviations

<b>ACU</b>	Automatic Calibration Unit
<b>BDT</b>	Boosted Decision Tree
<b>CD</b>	Central Detector
<b>CLS</b>	Cable Loop System
<b>CNN</b>	Convolutional NN
<b>DNN</b>	Deep NN
<b>GNN</b>	Graph NN
<b>GT</b>	Guiding Tube
<b>IBD</b>	Inverse Beta Decay
<b>IO</b>	Inverse Ordering
<b>JUNO</b>	Jiangmen Underground Neutrino Observatory
<b>LPMT</b>	Large PMT
<b>LS</b>	Liquid Scintillator
<b>MC</b>	Monte Carlo simulation
<b>ML</b>	Machine Learning
<b>NMO</b>	Neutrino Mass Ordering
<b>NN</b>	Neural Network
<b>NO</b>	Normal Ordering
<b>PE</b>	Photo Electron
<b>PMT</b>	Photo-Multipliers Tubes
<b>ROV</b>	Remotely Operated under-LS Vehicle
<b>SPMT</b>	Small PMT
<b>TR Area</b>	Total Reflexion Area
<b>TTS</b>	Time Transit Spread
<b>TT</b>	Top Tracker
<b>WCD</b>	Water Cherenkov Detector



# 4 Contents

5	<b>Contents</b>	1
6	<b>Remerciements</b>	3
7	<b>Introduction</b>	5
8	<b>1 Neutrino physics</b>	7
9	1.1 Standard model . . . . .	7
10	1.1.1 Limits of the standard model . . . . .	7
11	1.2 Historic of the neutrino . . . . .	7
12	1.3 Oscillation . . . . .	7
13	1.3.1 Phenomologies . . . . .	7
14	1.4 Open questions . . . . .	7
15	<b>2 The JUNO experiment</b>	9
16	2.1 Neutrinos physics in JUNO . . . . .	9
17	2.1.1 Reactor neutrino oscillation for NMO and precise measurements . . . . .	10
18	2.1.2 Other physics . . . . .	13
19	2.2 The JUNO detector . . . . .	14
20	2.2.1 Detection principle . . . . .	14
21	2.2.2 Central Detector (CD) . . . . .	16
22	2.2.3 Veto detector . . . . .	18
23	2.3 Calibration strategy . . . . .	19
24	2.3.1 Energy scale calibration . . . . .	19
25	2.3.2 Calibration system . . . . .	20
26	2.4 Satellite detectors . . . . .	21
27	2.4.1 TAO . . . . .	21
28	2.4.2 OSIRIS . . . . .	21
29	2.5 Software . . . . .	21
30	2.6 State of the art of the Offline IBD reconstruction in JUNO . . . . .	22
31	2.6.1 Interaction vertex reconstruction . . . . .	22
32	2.6.2 Energy reconstruction . . . . .	27
33	2.6.3 Machine learning for reconstruction . . . . .	29
34	2.7 JUNO sensitivity to NMO and precise measurements . . . . .	31
35	2.7.1 Fitting procedure . . . . .	32

---

36	<b>3 Machine learning and Artificial Neural Network</b>	33
37	3.1 History of the Machine learning . . . . .	33
38	3.2 Boosted Decision Tree (BDT) . . . . .	33
39	3.3 Artificial Neural Network (NN) . . . . .	33
40	3.3.1 Fully Connected Deep Neural Network (FCDNN) . . . . .	33
41	3.3.2 Convolutional Neural Network (CNN) . . . . .	33
42	3.3.3 Graph Neural Network (GNN) . . . . .	33
43	3.3.4 Adversarial Neural Network (ANN) . . . . .	33
44	<b>4 Image recognition for IBD reconstruction with the SPMT system</b>	35
45	<b>5 Graph representation of JUNO for IBD reconstruction with the LPMT system</b>	37
46	<b>6 Reliability of machine learning methods</b>	39
47	<b>7 Discrimination of e+/e- events in JUNO</b>	41
48	<b>8 Conclusion</b>	43
49	<b>Bibliography</b>	45

<sup>50</sup> **Remerciements**



# 51 Introduction



<sup>52</sup> **Chapter 1**

<sup>53</sup> **Neutrino physics**

<sup>54</sup>

*The neutrino, or  $\nu$  for the close friends, a fascinating and invisible particle. Some will say that dark matter also have those property but at least we are pretty confident that neutrinos exists.*

<sup>55</sup> **1.1 Standard model**

<sup>56</sup> **1.1.1 Limits of the standard model**

<sup>57</sup> **1.2 Historic of the neutrino**

<sup>58</sup> **First theories**

<sup>59</sup> **Discovery**

<sup>60</sup> **Milestones and anomalies**

<sup>61</sup> **1.3 Oscillation**

<sup>62</sup> **1.3.1 Phenomologies**

<sup>63</sup> **1.4 Open questions**

Decrire le m  
Regarder th  
Kochebina  
Limite du n  
Interessant,  
les neutrino  
CP ? Pb des



<sup>64</sup> **Chapter 2**

<sup>65</sup> **The JUNO experiment**

<sup>66</sup>

*"Ave Juno, rosae rosam, et spiritus rex". It means nothing but I found it in tone.*

<sup>67</sup>

The first idea of a medium baseline ( $\sim 52$  km) experiment, was explored in 2008 [1] where it was demonstrated that the Neutrino Mass Ordering (NMO) could be determined by a medium baseline experiment if  $\sin^2(2\theta_{13}) > 0.005$  without the requirements of accurate knowledge of the reactor antineutrino spectra and the value of  $\Delta m_{32}^2$ . From this idea is born the Jiangmen Underground Neutrino Observatory (JUNO) experiment.

<sup>72</sup>

JUNO is a neutrino detection experiment under construction located in China, in Guangdong proving, near the city of Kaiping. Its main objectives are the determination of the mass ordering at the  $3-4\sigma$  level in 6 years of data taking and the measurement at the sub-percent precision of the oscillation parameters  $\Delta m_{21}^2$ ,  $\sin^2 \theta_{12}$ ,  $\Delta m_{32}^2$  and with less precision  $\sin^2 \theta_{13}$  [2].



FIGURE 2.1 – On the left: Location of the JUNO experiment and its reactor sources in southern China. On the right: Aerial view of the experimental site

<sup>76</sup>

For this JUNO will measure the electronic anti-neutrinos ( $\bar{\nu}_e$ ) flux coming from the nuclear reactors of Taishan, Yangjiang, for a total power of  $26.6 \text{ GW}_{th}$ , and the Daya Bay power plant to a lesser extent. All of those cores are the second-generation pressurized water reactors CPR1000, which is a derivative of Framatome M310. Details about the power plants characteristics and their expected flux of  $\bar{\nu}_e$  can be found in the table 2.1. The distance of 53 km has been specifically chosen to maximize the disappearance probability of the  $\bar{\nu}_e$ . The data taking is scheduled to start early 2025.

<sup>82</sup>

## 2.1 Neutrinos physics in JUNO

<sup>83</sup>

Even if the JUNO design detailed in section 2.2 was optimized for the measurement of the NMO, its large detection volume, excellent energy resolution and background level and understanding make it also an excellent detector to measure the flux coming from other neutrino sources. Thus

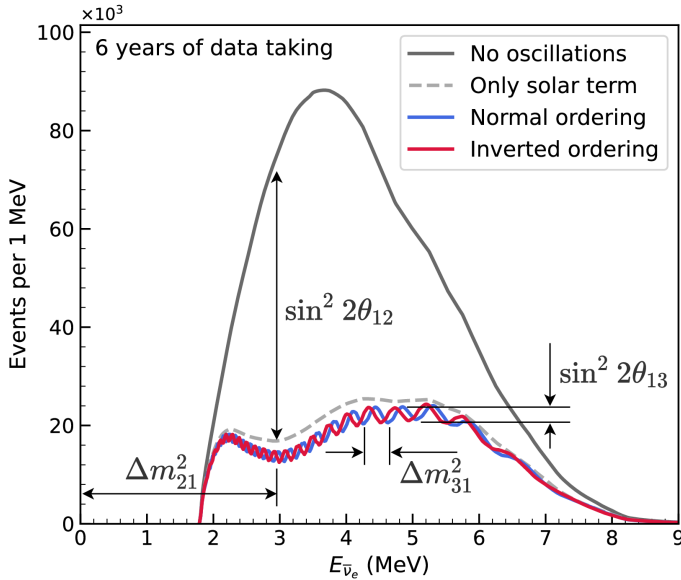


FIGURE 2.2 – Expected number of neutrinos event per MeV in JUNO after 6 years of data taking. The black curve shows the flux if there was no oscillation. The light gray curve shows the oscillation if only the solar terms are taken in account ( $\theta_{12}$ ,  $\Delta m_{21}^2$ ). The blue and red curve shows the spectrum in the case of, respectively, NO and IO. The dependency of the oscillation to the different parameters are schematized by the double sided arrows. We can see the NMO sensitivity by looking at the fine phase shift between the red and the blue curve.

<sup>86</sup> the scientific program of JUNO extends way over reactor antineutrinos. The following section is an  
<sup>87</sup> overview of the different physics topic JUNO will contribute in the coming years.

### <sup>88</sup> 2.1.1 Reactor neutrino oscillation for NMO and precise measurements

Previous works [1, 3] shows that oscillation parameters and the NMO can be observed by looking at the  $\bar{\nu}_e$  disappearance energy spectrum coming from medium baseline nuclear reactor. This disappearance probability can be expressed as [2] :

$$P(\bar{\nu}_e \rightarrow \bar{\nu}_e) = 1 - \sin^2 2\theta_{12} c_{13}^4 \sin^2 \frac{\Delta m_{21}^2 L}{4E} - \sin^2 2\theta_{13} \left[ c_{12}^2 \sin^2 \frac{\Delta m_{31}^2 L}{4E} + s_{12}^2 \sin^2 \frac{\Delta m_{32}^2 L}{4E} \right]$$

<sup>89</sup> Where  $s_{ij} = \sin \theta_{ij}$ ,  $c_{ij} = \cos \theta_{ij}$ ,  $E$  is the  $\bar{\nu}_e$  energy and  $L$  is the baseline. We can see the sensitivity  
<sup>90</sup> to the NMO in the dependency to  $\Delta m_{32}^2$  and  $\Delta m_{31}^2$  causing a phase shift of the spectrum as we can  
<sup>91</sup> see in the figure 2.2. By carefully adjusting a theoretical spectrum to the data, one can extract the  
<sup>92</sup> NMO and the oscillation parameters. The statistic procedure used to adjust the theoretical spectrum  
<sup>93</sup> is reviewed in more details in the section 2.7.1. To reach the desired sensitivity, JUNO must meet  
<sup>94</sup> multiple requirements but most notably:

- <sup>95</sup> 1. An energy resolution of  $3\% / \sqrt{E(\text{MeV})}$  to be able to distinguish the fine structure of the fast  
<sup>96</sup> oscillation.
- <sup>97</sup> 2. An energy precision of 1% in order to not err on the location of the oscillation pattern.
- <sup>98</sup> 3. A baseline of  $53 \pm 0.5$  km to maximise the  $\bar{\nu}_e$  oscillation probability.
- <sup>99</sup> 4. At least  $\approx 100,000$  events to limit the spectrum distortion due to statistical uncertainties.

100  **$\bar{\nu}_e$  flux coming from nuclear power plants**

101 To get such high measurements precision, it is necessary to have a very good understanding of  
 102 the sources characteristics. For its NMO and precise measurement studies, JUNO will observe the  
 103 energy spectrum of neutrinos coming from the nuclear power plants Taishan and Yangjiang's cores,  
 104 located at 53 km of the detector to maximise the disappearance probability of the  $\bar{\nu}_e$ .

Reactor	Power (GW <sub>th</sub> )	Baseline (km)	IBD Rate (day <sup>-1</sup> )	Relative Flux (%)
Taishan	9.2	52.71	15.1	32.1
Core 1	4.6	52.77	7.5	16.0
Core 2	4.6	52.64	7.6	16.1
Yangjiang	17.4	52.46	29.0	61.5
Core 1	2.9	52.74	4.8	10.1
Core 2	2.9	52.82	4.7	10.1
Core 3	2.9	52.41	4.8	10.3
Core 4	2.9	52.49	4.8	10.2
Core 5	2.9	52.11	4.9	10.4
Core 6	2.9	52.19	4.9	10.4
Daya Bay	17.4	215	3.0	6.4

TABLE 2.1 – Characteristics of the nuclear power plants observed by JUNO. The IBD rate are estimated from the baselines, the reactors full thermal power, selection efficiency and the current knowledge of the oscillation parameters

105 The  $\bar{\nu}_e$  coming from reactors are emitted from  $\beta$ -decay of unstable fission fragments. The Taishan  
 106 and Yangjiang reactors are Pressurised Water Reactor (PWR), the same type as Daya Bay. In those  
 107 type of reactor more the 99.7 % and  $\bar{\nu}_e$  are produced by the fissions of four fuel isotopes  $^{235}\text{U}$ ,  $^{238}\text{U}$ ,  
 108  $^{239}\text{Pu}$  and  $^{241}\text{Pu}$ . The neutrino flux per fission of each isotope is determined by the inversion of the  
 109 measured  $\beta$  spectra of fission product [4–8] or by calculation using the nuclear databases [9, 10].

110 The neutrino flux coming from a reactor at a time  $t$  can be predicted using

$$\phi(E_\nu, t)_r = \frac{W_{th}(t)}{\sum_i f_i(t) e_i} \sum_i f_i(t) S_i(E_\nu) \quad (2.1)$$

111 where  $W_{th}(t)$  is the thermal power of the reactor,  $f_i(t)$  is the fraction fission of the  $i$ th isotope,  $e_i$  its  
 112 thermal energy released in each fission and  $S_i(e_\nu)$  the neutrino flux per fission for this isotope. Using  
 113 this method, the flux uncertainty is expected to be of an order of 2-3 % [11].

114 In addition to those prediction, a satellite experiment named TAO[12] will be setup near the  
 115 reactor core Taishan-1 to measure with an energy resolution of 2% at 1 MeV the neutrino flux coming  
 116 from the core. It will help identifying unknown fine structure and give more insight on the  $\bar{\nu}_e$  flux  
 117 coming from this reactor.

118 One the open issue about reactor anti-neutrinos flux is the so-called neutrino anomaly [13], an  
 119 unexpected surplus of neutrino emission in the spectra around 5 MeV. Multiples scientists are trying  
 120 to explain this surplus by advanced recalculation of the nuclei model during beta decay [14, 15] but  
 121 no consensus on this issue has been reached yet.

122 **Background in the neutrinos reactor spectrum**

123 Considering the close reactor neutrinos flux as the main signal, the signals that are considered as  
 124 background are:

- 125 — The geoneutrinos producing background in the 0.511 ~ 2.7 MeV region.
- 126 — The neutrinos coming from the other nuclear reactors around Earth.

127 In addition to all those physics signal, non-neutrinos signal that would mimic an IBD will also be  
 128 present. It is composed of:

- The signal coming from radioactive decay ( $\alpha$ ,  $\gamma$ ,  $\beta$ ) from natural radioactive isotopes in the material of the detector.
- Cosmogenic event such as fast neutrons and activated isotopes induced by muons passing through the detector, most notably the spallation on  $^{12}\text{C}$ .
- All those events represent a non-negligible part of the spectrum as shown in figure 2.3.

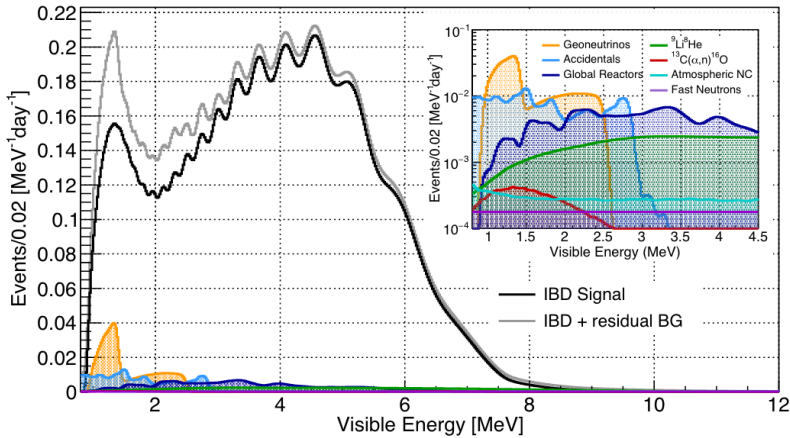


FIGURE 2.3 – Expected visible energy spectrum measured with the LPMT system with (grey) and without (black) backgrounds. The background amount for about 7% of the IBD candidate and are mostly localized below 3 MeV [11]

#### 134 Identification of the mass ordering

To identify the mass ordering, we adjust the theoretical neutrino energy spectrum under the two hypothesis of NO and IO. Those give us two  $\chi^2$ , respectively  $\chi^2_{NO}$  and  $\chi^2_{IO}$ . By computing the difference  $\Delta\chi^2 = \chi^2_{NO} - \chi^2_{IO}$  we can determine the most probable mass ordering and the confidence interval: NO if  $\Delta\chi^2 > 0$  and IO if  $\Delta\chi^2 < 0$ . Current studies shows that the expected sensitivity the mass ordering would be of  $3.4\sigma$  after 6 years of data taking in nominal setup[2]. More detailed explanations about the procedure can be found in the section 2.7.1.

#### 141 Precise measurement of the oscillations parameters

The oscillations parameters  $\theta_{12}$ ,  $\theta_{13}$ ,  $\Delta m_{21}^2$ ,  $\Delta m_{31}^2$  are free parameters in the fit of the oscillation spectrum. The precision on those parameters have been estimated and are shown in table 2.2. We see that for  $\theta_{12}$ ,  $\Delta m_{21}^2$ ,  $\Delta m_{31}^2$ , precision at 6 years is better than the reference precision by an order of magnitude [11]

	Central Value	PDG 2020	100 days	6 years	20 years
$\Delta m_{31}^2 (\times 10^{-3} \text{ eV}^2)$	2.5283	$\pm 0.034$ (1.3%)	$\pm 0.021$ (0.8%)	$\pm 0.0047$ (0.2%)	$\pm 0.0029$ (0.1%)
$\Delta m_{21}^2 (\times 10^{-3} \text{ eV}^2)$	7.53	$\pm 0.18$ (2.4%)	$\pm 0.074$ (1.0%)	$\pm 0.024$ (0.3%)	$\pm 0.017$ (0.2%)
$\sin^2 \theta_{12}$	0.307	$\pm 0.013$ (4.2%)	$\pm 0.0058$ (1.9%)	$\pm 0.0016$ (0.5%)	$\pm 0.0010$ (0.3%)
$\sin^2 \theta_{13}$	0.0218	$\pm 0.0007$ (3.2%)	$\pm 0.010$ (47.9%)	$\pm 0.0026$ (12.1%)	$\pm 0.0016$ (7.3%)

TABLE 2.2 – A summary of precision levels for the oscillation parameters. The reference value (PDG 2020 [16]) is compared with 100 days, 6 years and 20 years of JUNO data taking.

### 2.1.2 Other physics

While the design of JUNO is tailored to measure  $\bar{\nu}_e$  coming from nuclear reactor, JUNO will be able to detect neutrinos coming from other sources thus allowing for a wide range of physics studies as detailed in the table 2.3 and in the following sub-sections.

Research	Expected signal	Energy region	Major backgrounds
Reactor antineutrino	60 IBDs/day	0–12 MeV	Radioactivity, cosmic muon
Supernova burst	5000 IBDs at 10 kpc 2300 elastic scattering	0–80 MeV	Negligible
DSNB (w/o PSD)	2–4 IBDs/year	10–40 MeV	Atmospheric $\nu$
Solar neutrino	hundreds per year for $^8B$	0–16 MeV	Radioactivity
Atmospheric neutrino	hundreds per year	0.1–100 GeV	Negligible
Geoneutrino	$\approx 400$ per year	0–3 MeV	Reactor $\nu$

TABLE 2.3 – Detectable neutrino signal in JUNO and the expected signal rates and major background sources

### 150 Geoneutrinos

151 Geoneutrinos designate the antineutrinos coming from the decay of long-lived radioactive elements 152 inside the Earth. The 1.8 MeV threshold necessary for the IBD makes it possible to measure 153 geoneutrinos from  $^{238}\text{U}$  and  $^{232}\text{Th}$  decay chains. The studies of geoneutrinos can help refine the Earth 154 crust models but is also necessary to characterise their signal, as they are a background to the mass 155 ordering and oscillations parameters studies.

### 156 Atmospheric neutrinos

157 Atmospheric neutrinos are neutrinos originating from the decay of  $\pi$  and  $K$  particles that are 158 produced in extensive air showers initiated by the interactions of cosmic rays with the Earth atmosphere. 159 Earth is mostly transparent to neutrinos below the PeV energy, thus JUNO will be able to 160 see neutrinos coming from all directions. Their baseline range is large (15km  $\sim$  13000km), they can 161 have energy between 0.1 GeV and 10 TeV and will contain all neutrino and antineutrinos flavour. 162 Their studies is complementary to the reactor antineutrinos and can help refine the constraints on 163 the NMO [2].

### 164 Supernovae burst neutrinos

165 Neutrinos are crucial component during all stages of stellar collapse and explosion. Detection 166 of neutrinos coming for core collapse supernovae will provide us important informations on the 167 mechanisms at play in those events. Thanks to its 20 kt sensible volume, JUNO has excellent capabilities 168 to detect all flavour of the  $\mathcal{O}(10 \text{ MeV})$  postshock neutrinos, and using neutrinos of the  $\mathcal{O}(1 \text{ MeV})$  will give 169 informations about the pre-supernovae neutrinos. All those informations will allow 170 to disentangle between the multiple hydro-dynamic models that are currently used to describe the 171 different stage of core-collapse supernovae.

### 172 Diffuse supernovae neutrinos background

173 Core-collapse supernovae in our galaxy are rare events, but they frequently occur throughout the 174 visible Universe sending burst of neutrinos in direction of the Earth. All those events contributes to 175 a low background flux of low-energy neutrinos called the Diffuse Supernovae Neutrino Background 176 (DSNB). Its flux and spectrum contains informations about the red-shift dependent supernovae rate,

177 the average supernovae neutrino energy and the fraction of black-hole formation in core-collapse supernovae. Depending of the DSNB model, we can expect 2-4 IBD events per year in the energy range  
 178 above the reactor  $\bar{\nu}_e$  signal, which is competitive with the current Super-Kamiokande+Gadolinium  
 179 phase [17].  
 180

### 181 Beyond standard model neutrinos interactions

182 JUNO will also be able to probe for beyond standard model neutrinos interactions. After the  
 183 main physics topics have been accomplished, JUNO could be upgraded to probe for neutrinoless  
 184 beta decay ( $0\nu\beta\beta$ ). The detection of such event would give critical informations about the nature  
 185 of neutrinos, is it a majorana or a dirac particle. JUNO will also be able to probe for neutrinos that  
 186 would come for the decay or annihilation of Dark Matter inside the sun and neutrinos from putative  
 187 primordial black hole. Through the unitary test of the mixing matrix, JUNO will be able to search  
 188 for light sterile neutrinos. Thanks to JUNO sensitivity, multiple other exotic can be performed on  
 189 neutrino related beyond standard model interactions.

## 190 2.2 The JUNO detector

191 The JUNO detector is a scintillator detector buried 693.35 meters under the ground (1800 meters  
 192 water equivalent). It consist of Central Detector (CD), a water pool and a Top Tracker (TT) as showed  
 193 in figure 2.4a. The CD is an acrylic vessel containing the 20 ktons of Liquid Scintillator (LS). It is  
 194 supported by a stainless steel structure and is immersed in that water pool that is used as shielding  
 195 from external radiation and as a cherenkov detector for the background. The top of the experiment  
 196 is partially covered by the Top Tracker (TT), a plastic scintillator detector which is use to detect the  
 197 atmospheric muons background and is acting as a veto detector.

198 The top of the experiment also host the LS purification system, a water purification system, a  
 199 ventilation system to get rid of the potential radon in the air. The CD is observed by two system of  
 200 Photo-Multipliers Tubes (PMT). They are attached to the steel structure and their electronic readout  
 201 is submersed near them. A third system of PMT is also installed on the structure but are facing  
 202 outward of the CD, instrumenting the water to be cherenkov detector. The CD and the cherenkov  
 203 detector are optically separated by Tyvek sheet. A chimney for LS filling and purification and for  
 204 calibration operations connects the CD to the experimental hall from the top.

205 The CD has been dimensioned to meet the requirements presented in section 2.1.1:

- 206 — Its 20 ktons monolithic LS provide a volume sizeable enough, in combination with the ex-  
 207 pected  $\bar{\nu}_e$  flux, to reach the desired statistic in 6 years. Its monolithic nature also allow for a  
 208 full containment of most of the events, preventing the energy loss in non-instrumented parts  
 209 that would arise from a segmented detector.
- 210 — Its large overburden shield it from most of the atmospheric background that would pollute  
 211 the signal.
- 212 — The localization of the experiment, chosen to maximize the disappearance with a 53km base-  
 213 line and in a region that allow two nuclear power plant to be used as sources.

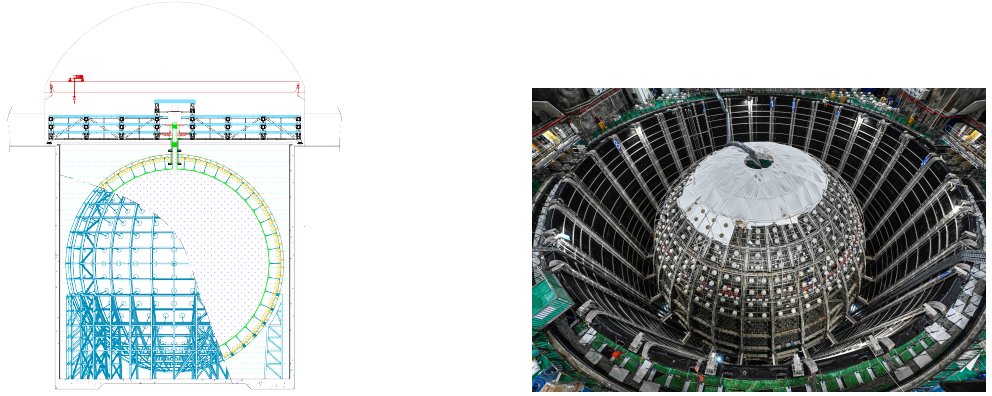
214 This section cover in details the different components of the detector and the detection systems.

### 215 2.2.1 Detection principle

The CD will detect the neutrino and measure their energy mainly via an Inverse Beta Decay (IBD) interaction with proton mainly from the  $^{12}\text{C}$  and H nucleus in the LS:

$$\bar{\nu}_e + p \rightarrow n + e^+$$

216 Kinematics calculation shows that this interaction has an energy threshold for the  $\bar{\nu}_e$  of  $(m_n + m_e -$   
 217  $m_p) \approx 1.806 \text{ MeV}$  [18] where  $m_\lambda$  is the mass of the  $\lambda$  particle. This threshold make the experiment



(A) Schematics view of the JUNO detector.

(B) Top down view of the JUNO detector under construction

218 blind to very low energy neutrinos. The residual energy  $E_\nu - 1.806$  MeV is be distributed as kinetic  
 219 energy between the positron and the neutron. The energy of the emitted positron  $E_e$  is given by [18]

$$E_e = \frac{(E_\nu - \delta)(1 + \epsilon_\nu) + \epsilon_\nu \cos \theta \sqrt{(E_\nu - \delta)^2 + \kappa m_e^2}}{\kappa} \quad (2.2)$$

220 where  $\kappa = (1 + \epsilon_\nu)^2 - \epsilon_\nu^2 \cos^2 \theta \approx 1$ ,  $\epsilon_\nu = \frac{E_\nu}{m_p} \ll 1$  and  $\delta = \frac{m_n^2 - m_p^2 - m_e^2}{2m_p} \ll 1$ . We can see from this  
 221 equation that the positron energy is strongly correlated to the neutrino energy.

222 The positron and the neutron will then propagate in the detection medium, the Liquid Scintillator  
 223 (LS), loosing their kinetic energy by exciting the molecule of the LS (more details in section 2.2.2).  
 224 Once stopped, the positron will annihilate with an electron from the medium producing two 511  
 225 KeV gamma. Those gamma will themselves interact with the LS, exciting it before being absorbed  
 226 by photoelectrical effect. The neutron will be captured by an hydrogen, emitting a 2.2 MeV gamma  
 227 in the process. This gamma will also deposit its energy before being absorbed by the LS.

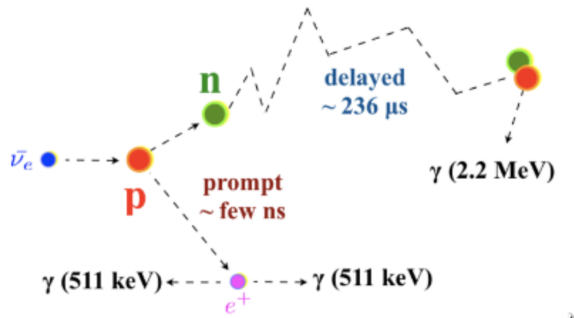


FIGURE 2.5 – Schematics of an IBD interaction in the central detector of JUNO

228 The scintillation photons have frequency in the UV and will propagate in the LS, being re-absorbed  
 229 and re-emitted by compton effect before finally be captured by PMTs instrumenting the acrylic  
 230 sphere. The analog signal of the PMTs digitized by the electronic is the signal of our experiment.  
 231 The signal produced by the positron is subsequently called the prompt signal, and the signal coming  
 232 from the neutron the delayed signal. This naming convention come from the fact that the positron  
 233 will deposit its energy rather quickly (few ns) where the neutron will take a bit more time ( $\sim 236$   $\mu$ s).

### 2.2.2 Central Detector (CD)

The central detector, composed of 20 ktons of Liquid Scintillator (LS), is the main part of JUNO. The LS is contained in a spherical acrylic vessel supported by a stainless steel structure. The CD and its structural support are submerged in a cylindrical water pool of 43.5m diameter and 44m height. We're confident that the water pool provide sufficient buffer protection in every direction against the rock radioactivity.

#### Acrylic vessel

The acrylic vessel is a spherical vessel of inner diameter of 35.4 m and a thickness of 120 mm. It is assembled from 265 acrylic panels, thermo bonded together. The acrylic recipes has been carefully tuned with extensive R&D to ensure it does not include plasticizer and anti-UV material that would stop the scintillation photons. Those panels requires to be pure of radioactive materials to not cause background. Current setup where the acrylic panels are molded in cleanrooms of class 10000, let us reach a uranium and thorium contamination of <0.5 ppt. The molding and thermoforming processes is optimized to increase the assemblage transparency in water to >96%. The acrylic vessel is supported by a stainless steel structure via supporting node (fig 2.6). The structure and the nodes are designed to be resilient to natural catastrophic events such as earthquake and can support many times the effective load of the acrylic vessel.

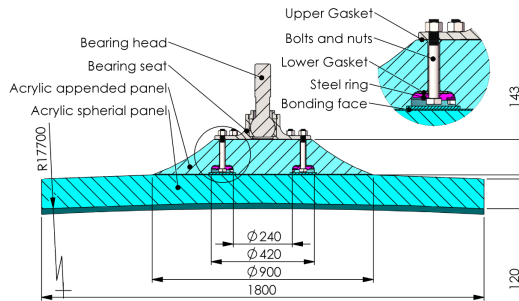


FIGURE 2.6 – Schematics of the supporting node for the acrylic vessel

#### Liquid scintillator

The Liquid Scintillator (LS) has a similar recipe as the one used in Daya Bay [19] but without gadolinium doping. It is made of three components, necessary to shift the wavelength of emitted photons to prevent their reabsorption:

1. The detection medium, the *linear alkylbenzene* (LAB). Selected because of its excellent transparency, high flash point, low chemical reactivity and good light yield. Accounting for  $\sim 98\%$  of the LS, it is the main component with which ionizing particles and gamma interact. Charged particles will collide with its electronic cloud transferring energy to the molecules, gamma will interact via compton effect with the electronic cloud before finally be absorbed via photoelectric effect.
2. The second component of the LS is the *2,5-diphenyloxazole* (PPO). A fraction of the excitation energy of the LAB is transferred to the PPO, mainly via non radiative process [20]. The PPO molecules de-excites in the same way, transferring their energy to the bis-MSB. The PPO makes for 1.5 % of the LS.
3. The last component is the *p-bis(o-methylstyryl)-benzene* (bis-MSB). Once excited by the PPO, it will emit photon with an average wavelength of  $\sim 430$  nm (full spectrum in figure 2.7) that can be detected by our photo-multipliers systems. It amount for  $\sim 0.5\%$  of the LS.

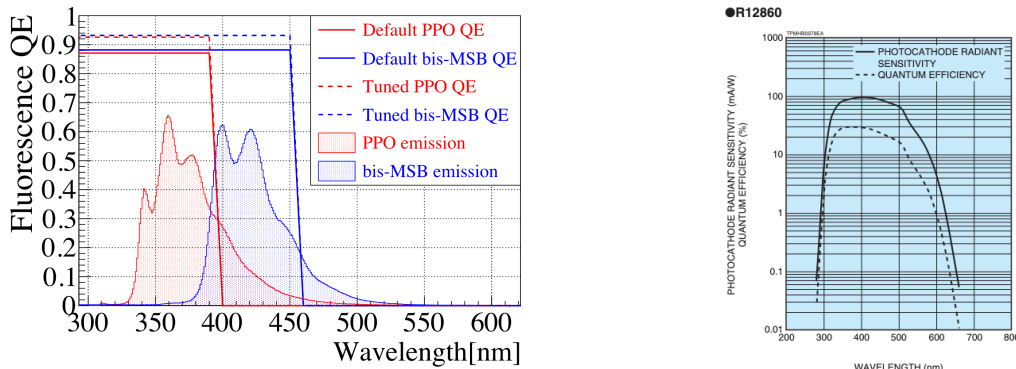


FIGURE 2.7 – On the left: Quantum efficiency (QE) and emission spectrum of the LAB and the bis-MSB [19]. On the right: Sensitivity of the Hamamatsu LPMT depending on the wavelength of the incident photons [21].

This formula has been optimized using dedicated studies with a Daya Bay detector [19, 22] to reach the requirements for the JUNO experiment:

- A light yield / MeV of the amount of  $10^4$  photons to maximize the statistic in the energy measurement.
- An attenuation length comparable to the size of the detector to prevent losing photons during their propagation in the LS. The final attenuation length is 25.8m [23] to compare with the CD diameter of 35.4m.
- Uranium/Thorium radiopurity to prevent background signal. The reactor neutrino program require a contamination fraction  $F < 10^{-15}$  while the solar neutrino program require  $F < 10^{-17}$ .

The LS will frequently be purified and tested in the Online Scintillator Internal Radioactivity Investigation System (OSIRIS) [24] to ensure that the requirements are kept during the lifetime of the experiment.

### Large Photo-Multipliers Tubes (PMTs)

The scintillation light produced by the LS is then collected by Photo-Multipliers Tubes (PMT) that transform the incoming photon into an electric signal. As described in figure 2.8, the incident photons interact with the photocathode via photoelectric effect producing an electron called a Photo-Electron (PE). This PE is then focused on the dynodes where the high voltage will allow it to be multiplied. After multiple amplification the resulting charge - in coulomb [C] - is collected by the anode and the resulting electric signal can be digitalized by the readout electronics from which the charge and timing can be extracted.

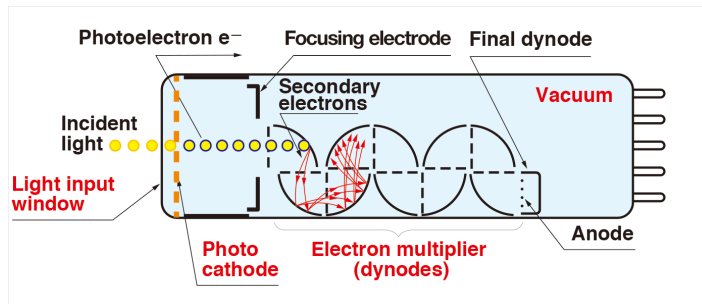


FIGURE 2.8 – Schematic of a PMT

The Large Photo-Multipliers Tubes (LPMT), used in the central detector and in the water pool, are 20-inch (50.8 cm) radius PMTs.  $\sim 5000$  dynode-PMTs [21] were produced by the Hamamatsu<sup>©</sup> company and  $\sim 15000$  Micro-Channel Plate (MCP) [25] by the NNVT<sup>©</sup> company. This system is the one responsible for the energy measurement with a energy resolution of  $3\%/\sqrt{E}$ , resolution necessary for the mass ordering measurement. To reach this precision, the system is composed of 17612 PMTs quasi uniformly distributed over the detector for a coverage of 75.2% reaching  $\sim 1800$  PE/MeV or  $\sim 2.3\%$  resolution due to statistic, leaving  $\sim 0.7\%$  for the systematic uncertainties. They are located outside the acrylic sphere in the water pool facing the center of the detector. To maintain the resolution over the lifetime of the experiment, JUNO require a failure rate  $< 1\%$  over 6 years.

The LPMTs electronic are divided in two parts. One "near", located underwater, in proximity of the LPMT to reduce the cable length between the PMT and early electronic. A second one, outside of the detector that is responsible for higher level analysis before sending the data to the DAQ.

The light yield per MeV induce that a LPMT can collect between 1 and 1000 PE per event, causing non linearity in the PMT response that need to be understood and calibrated, see section 2.3 for more details.

#### 304 Small Photo-Multipliers Tubes (SPMTs)

The Small PMT (SPMTs) system is made of 3-inch (7.62 cm) PMTs. They will be used in the CD as a secondary detection system. Those 25600 SPMTs will observe the same events as the LPMTs, thus sharing the physics and detector systematics up until the photon conversion. With a detector coverage of 2.7%, this system will collect  $\sim 43$  PE/MeV for a final energy resolution of  $\sim 17\%$ . This resolution is not enough to measure the NMO,  $\theta_{13}$ ,  $\Delta m_{31}^2$  but will be sufficient to independently measure  $\theta_{12}$  and  $\Delta m_{21}^2$ .

Due to the low PE rate, SPMTs will be running in photo-counting mode in the reactor range and thus will be insensitive to non-linearity effect. Using this property, the intrinsic charge non linearity of the LPMTs can be measured by comparing the PE count in the SPMTs and LPMTs [26]. Also, due to their smaller size and electronics, SPMTs have a better timing resolutions than the LPMTs. At higher energy range, like supernovae events, LPMTs will saturate where SPMTs due to their lower PE collection will to produce a reliable measure of the energy spectrum.

The Data Acquisition System (DAQ) is designed to support the event rate of IBD, background, dark noise and supplementary storage buffers are present in the LPMT electronics to withstand the event rate during supernovae burst.

#### 320 2.2.3 Veto detector

The CD will be bathed in constant background noise coming from numerous sources : the radioactivity from surrounding rock and its own components or from the flux of cosmic muons. This background needs to be rejected to ensure the purity of the IBD spectrum. To prevent a big part of them, JUNO use two veto detector that will tag events as background before CD analysis.

#### 325 Cherenkov in water pool

The Water Cherenkov Detector (WCD) is the instrumentation of the water buffer around the CD. When high speed charged particles will pass through the water, they will produced cherenkov photons. The light will be collected by 2400 MCP LPMTs installed on the outer surface of the CD structure. The muons veto strategy is based on a PMT multiplicity condition. WCD PMTs are grouped in ten zones: 5 in the top, 5 in the bottom. A veto is raised either when more than 19 PMTs are triggered in one zone or when two adjacent zones simultaneously trigger more than 13 PMTs. Using this trigger, we expect to reach a muon detection efficiency of 99.5% while keeping the noise at reasonable level.

334 **Top tracker**

335 The JUNO Top Tracker (TT) is a plastic scintillator detector located on the top of the experiment  
 336 (see figure 2.9). Made from plastic scintillator from OPERA [27] layered horizontally in 3 layers on  
 337 the top of the detector, the TT will be able to detect incoming atmospheric muons. With its coverage,  
 338 about 1/3 of the of all atmospheric muons that passing through the CD will also pass through the 3  
 339 layer of the detector. While it does not cover the majority of the CD, the TT is particularly effective  
 340 to detect muons coming through the filling chimney region which might present difficulties from the  
 341 other subsystems in some classes of events.

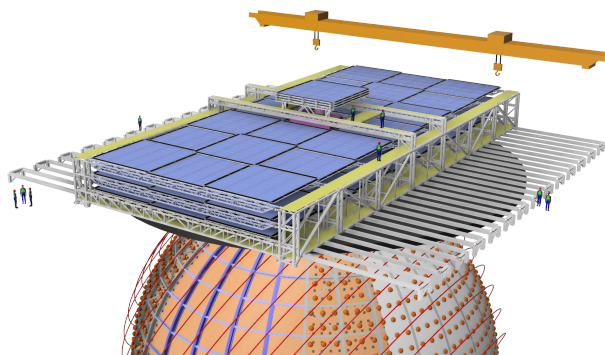


FIGURE 2.9 – The JUNO top tracker

341

342 **2.3 Calibration strategy**

343 The calibration is a crucial part of the JUNO experiment. Because we are looking at civil reactor  
 344 neutrino it might be impossible to run measurement without signal, it would need to shut down  
 345 every reactor from the Taishan and Yangjiang power plants which is realistically impossible. Because  
 346 of this continuous rate, low frequency signal event, we need high frequency, recognisable sources in  
 347 the energy range of interest : [0-12] MeV for the positron signal and 2.2 MeV for the neutron capture.  
 348 It is expected that the CD response will be different depending on the type of particle, due to the  
 349 interaction with LS, the position on the event and the optical response of the acrylic sphere (see  
 350 section 2.6). We also expect a non-linear energy response of the CD due to the LS properties [19] but  
 351 also due to the saturation of the LPMTs system when collecting a large amount of PE [26].

352 **2.3.1 Energy scale calibration**

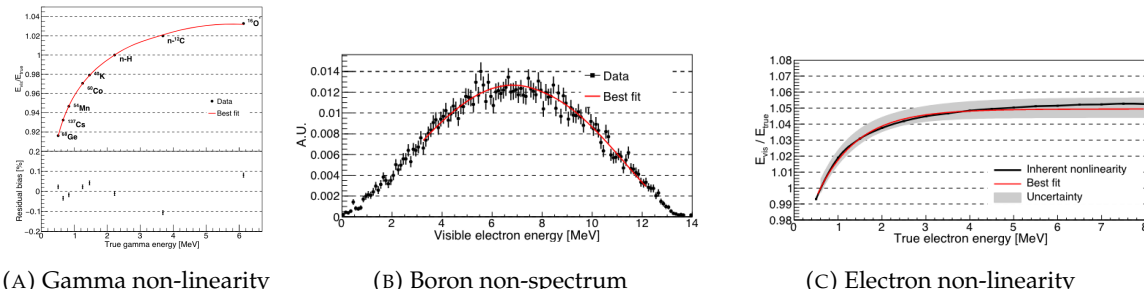
353 While electrons and positrons sources would be ideal, for a large LS detector thin-walled electrons  
 354 or positrons sources could lead to leakage of radionucleides causing radioactive contamination.  
 355 Instead, we consider gamma sources in the range of the prompt energy of IBDs. The sources are  
 356 reported in table 2.4.

357 For the  $^{68}\text{Ge}$  source, it will decay in  $^{68}\text{Ga}$  via electron capture, which will itself  $\beta^+$  decay into  $^{68}\text{Zn}$ .  
 358 The positrons will be absorbed by the enclosure so only the annihilation gamma will be released. In  
 359 addition,  $(\alpha, n)$  sources like  $^{241}\text{Am-Be}$  and  $^{241}\text{Am-}^{13}\text{C}$  are used to provide both high energy gamma  
 360 and neutrons, which will later be captured in the LS producing the 2.2 MeV gamma.

361 From this calibration we call  $E_{\text{vis}}$  the "visible energy" that is reconstructed by our current algo-  
 362 rithms and we compare it to the true energy deposited by the calibration source. The results shown  
 363 in figure 2.10 show the expected response of the detector from calibration sources. The non-linearity  
 364 is clearly visible from the  $E_{\text{vis}}/E_{\text{true}}$  shape. See [28] for more details.

Sources / Processes	Type	Radiation
$^{137}\text{Cs}$	$\gamma$	0.0662 MeV
$^{54}\text{Mn}$	$\gamma$	0.835 MeV
$^{60}\text{Co}$	$\gamma$	1.173 + 1.333 MeV
$^{40}\text{K}$	$\gamma$	1.461 MeV
$^{68}\text{Ge}$	$e^+$	annihilation 0.511 + 0.511 MeV
$^{241}\text{Am-Be}$	$n, \gamma$	neutron + 4.43 MeV ( $^{12}\text{C}^*$ )
$^{241}\text{Am-}^{13}\text{C}$	$n, \gamma$	neutron + 6.13 MeV ( $^{16}\text{O}^*$ )
$(n, \gamma)p$	$\gamma$	2.22 MeV
$(n, \gamma)^{12}\text{C}$	$\gamma$	4.94 MeV or 3.68 + 1.26 MeV

TABLE 2.4 – List of sources and their process considered for the energy scale calibration

FIGURE 2.10 – Fitted and simulated non linearity of gamma, electron sources and from the  $^{12}\text{B}$  spectrum. Black points are simulated data. Red curves are the best fits

### 2.3.2 Calibration system

The non-uniformity due to the event position in the detector (more details in section 2.6) will be studied using multiples systems that are schematized in figure 2.11. They allow to position sources at different location in the CD.

- For a one-dimension vertical calibration, the Automatic Calibration Unit (ACU) will be able to deploy multiple radioactive sources or a pulse laser diffuser ball along the central axis of the CD through the top chimney. The source position precision is less than 1cm.
- For off-axis calibration, a calibration source attached to a Cable Loop System (CLS) can be moved on a vertical half-plane by adjusting the length of two connection cable. Two set of CSL will be deployed to provide a 79% effective coverage of a vertical plane.
- A Guiding Tube (GT) will surround the CD to calibrate the non-uniformity of the response at the edge of the detector
- A Remotely Operated under-LS Vehicle (ROV) can be deployed to desired location inside LS for a more precise and comprehensive calibration. The ROV will also be equipped with a camera for inspection of the CD.

The preliminary calibration program is depicted in table 2.5.

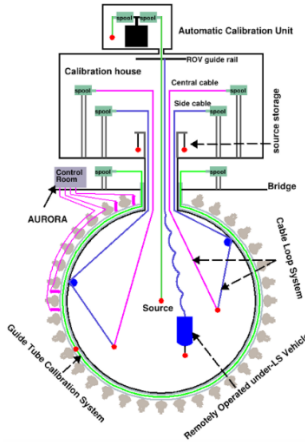


FIGURE 2.11 – Overview of the calibration system

Program	Purpose	System	Duration [min]
Weekly calibration	Neutron (Am-C)	ACU	63
	Laser	ACU	78
Monthly calibration	Neutron (Am-C)	ACU	120
	Laser	ACU	147
	Neutron (Am-C)	CLS	333
	Neutron (Am-C)	GT	73
Comprehensive calibration	Neutron (Am-C)	ACU, CLS and GT	1942
	Neutron (Am-Be)	ACU	75
	Laser	ACU	391
	$^{68}\text{Ge}$	ACU	75
	$^{137}\text{Cs}$	ACU	75
	$^{54}\text{Mn}$	ACU	75
	$^{60}\text{Co}$	ACU	75
	$^{40}\text{K}$	ACU	158

TABLE 2.5 – Calibration program of the JUNO experiment

## 381 2.4 Satellite detectors

### 382 2.4.1 TAO

#### 383 Objectives

#### 384 Detector

### 385 2.4.2 OSIRIS

#### 386 Objectives

#### 387 Detector

## 388 2.5 Software

389 The simulation, reconstruction and analysis algorithms are all packaged in the JUNO software,  
 390 subsequently called the software. It is composed of multiple components integrated in the SNiPER  
 391 [29] framework:

- Various primary particles simulators for the different kind of events, background and calibration sources.
- A Geant4 [30–32] Monte Carlo (MC) simulation containing the detectors geometries, a custom optical model for the LS and the supporting structures of the detectors. The Geant4 simulation integrate all relevant physics process for JUNO, validated by the collaboration. This step of the simulation is commonly called *Detsim* and compute up to the production of photo-electrons in the PMTs. The optics properties of the different materials and detector components have been measured beforehand to be used to define the material and surfaces in the simulation.
- An electronic simulation, simulating the response waveform of the PMTs, tracking it through the digitization process, accounting for effects such as non-linearity, dark noise, Time Transit Spread (TTS), pre-pulsing, after-pulsing and ringing if the waveform. It's also the step handling the event triggers and mixing. This step is commonly referenced as *Elecsim*.
- A waveform reconstruction where the digitized waveform are filtered to remove high-frequency white noise and then deconvoluted to yield time and charge informations of the photons hits on the PMTs. This step is commonly referenced as *Calib*.
- The charge and time informations are used by reconstruction algorithms to reconstruct the interaction vertex and the deposited energy. This step is commonly reported as *Reco*. See section 2.6 for more details on the reconstruction.
- Once the singular events are reconstructed, they go through event pairing and classification to select IBD events. This step is named Event Classification.
- The purified signal is then analysed by the analysis framework which depend of the physics topic of interest.

The steps Reco and Event Classification are divided into two category of algorithm. Fast but less accurate algorithms that are running during the data taking designated as the *Online* algorithms. Those algorithm are used to take the decision to save the event on tape or to throw it away. More accurate algorithms that run on batch of events designated *Offline* algorithms. They are used for the physics analysis. The Offline Reco will be one of the main topic of interest for this thesis.

## 2.6 State of the art of the Offline IBD reconstruction in JUNO

The main reconstruction method currently run in JUNO is a data-driven method based on a likelihood maximization [33, 34] using only the LPMTs. The first step is to reconstruct the interaction vertex from which the energy reconstruction is dependent. It is also necessary for event pairing and classification.

### 2.6.1 Interaction vertex reconstruction

To start the likelihood maximization, a rough estimation of the vertex and of the event timing is needed. We start by estimating the vertex position using a charge based algorithm.

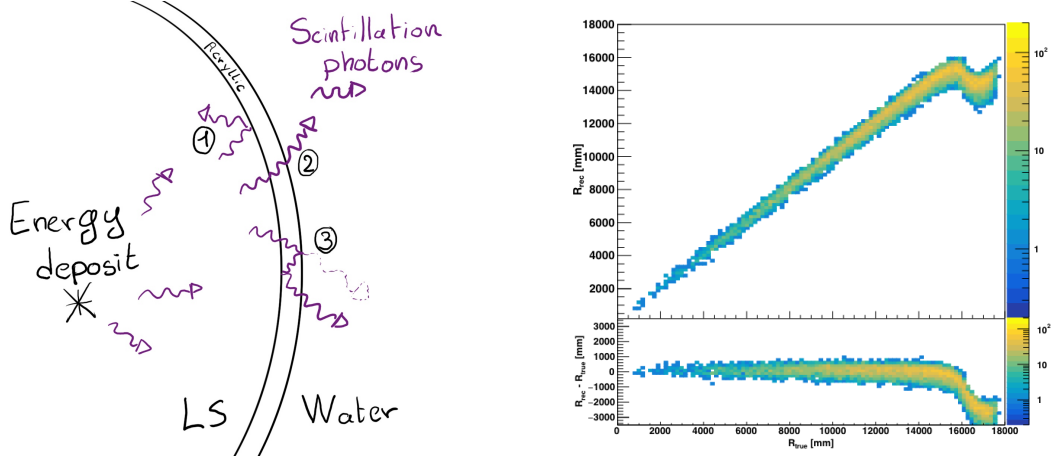
#### Charge based algorithm

The charge-based algorithm is basically base on the charge-weighted average of the PMT position.

$$\vec{r}_{cb} = a \cdot \frac{\sum_i q_i \cdot \vec{r}_i}{\sum_i q_i} \quad (2.3)$$

Where  $q_i$  is the reconstructed charge of the pulse of the  $i$ th PMT and  $\vec{r}_i$  is its position.  $\vec{r}_0$  is the reconstructed interaction position.  $a$  is a scale factor introduced because a weighted average over a 3D sphere is inherently biased. Using calibration we can estimate  $a \approx 1.3$  [35]. The results in figure 2.12b shows that the reconstruction is biased from around 15m and further. This is due to the phenomena called “total reflection area” or TR Area.

434 As depicted in the figure 2.12a the optical photons, given that they have a sufficiently large  
 435 incidence angle, can be deviated of their trajectories when passing through the interfaces LS-acrylic  
 436 and water-acrylic due to the optical index difference. This cause photons to be lost or to be detected  
 437 by PMT further than anticipated if we consider their rectilinear trajectories. This cause the charge  
 438 barycenter the be located closer to the center than the event really is.



(A) Illustration of the different optical photons reflection scenarios. 1 is the reflection of the photon at the interface LS-acrylic or acrylic-water. 2 is the transmission of the photons through the interfaces. 3 is the conduction of the photon in the acrylic.

(B) Heatmap of  $R_{rec}$  and  $R_{rec} - R_{true}$  as a function of  $R_{true}$  for 4MeV prompt signals uniformly distributed in the detector calculated by the charge based algorithm

FIGURE 2.12

439 It is to be noted that charge based algorithm, in addition to be biased near the edge of the detector,  
 440 does not provide any information about the timing of the event. Therefore, a time based algorithm  
 441 needs to be introduced to provide initial values.

#### 442 Time based algorithm

443 The time based algorithm use the distribution of the time of flight corrections  $\Delta t$  (Eq 2.4) of an  
 444 event to reconstruct its vertex and  $t_0$ . It follow the following iterations:

- 445 1. Use the charge based algorithm to get an initial vertex to start the iteration.  
 446 2. Calculate the time of flight correction for the  $i$ th PMT using

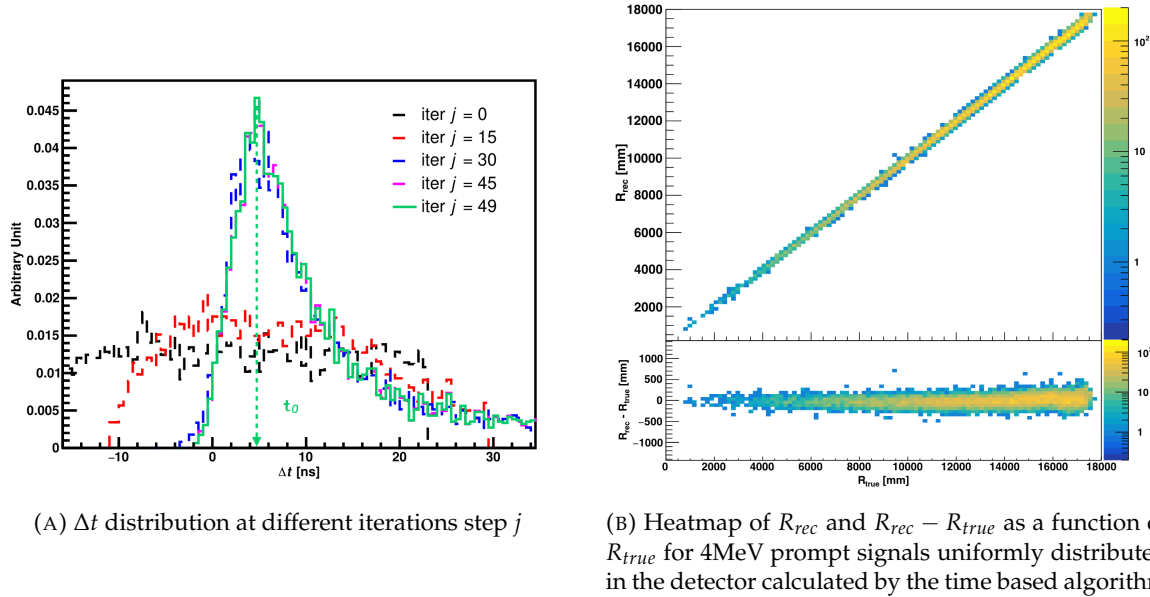
$$\Delta t_i(j) = t_i - \text{tof}_i(j) \quad (2.4)$$

447 where  $j$  is the iteration step,  $t_i$  is the timing of the  $i$ th PMT, and  $\text{tof}_i$  is the time-of-flight of the  
 448 photon considering an rectilinear trajectory and an effective velocity in the LS and water (see  
 449 [35] for detailed description of this effective velocity). Plot the  $\Delta t$  distribution and label the  
 450 peak position as  $\Delta t^{\text{peak}}$  (see fig 2.13a).

- 451 3. Calculate a correction vector  $\vec{\delta}[\vec{r}(j)]$  as

$$\vec{\delta}[\vec{r}(j)] = \frac{\sum_i \left( \frac{\Delta t_i(j) - \Delta t^{\text{peak}}(j)}{\text{tof}_i(j)} \right) \cdot (\vec{r}_0(j) - \vec{r}_i)}{N^{\text{peak}}(j)} \quad (2.5)$$

452 where  $\vec{r}_0$  is the vertex position at the beginning of this iteration,  $\vec{r}_i$  is the position of the  $i$ th  
 453 PMT. To minimize the effect of scattering, dark noise and reflection, only the pulse happening

(A)  $\Delta t$  distribution at different iterations step  $j$ (B) Heatmap of  $R_{rec}$  and  $R_{rec} - R_{true}$  as a function of  $R_{true}$  for 4MeV prompt signals uniformly distributed in the detector calculated by the time based algorithm

in a time window (-10 ns, +5 ns) around  $\Delta t^{\text{peak}}$  are considered.  $N^{\text{peak}}$  is the number of PE collected in this time-window.

456     4. if  $\vec{\delta}[\vec{r}(j)] < 1\text{mm}$  or  $j \geq 100$ , stop the iteration. Otherwise  $\vec{r}_0(j+1) = \vec{r}_0(j) + \vec{\delta}[\vec{r}(j)]$  and go to  
457     step 2.

458     However because the earliest arrival time is used,  $t_i$  is related to the number photoelectrons  $N_i^{\text{pe}}$   
459     detected by the PMT [36–38]. To reduce bias in the vertex reconstruction, the following equation is  
460     used to correct  $t_i$  into  $t'_i$ :

$$t'_i = t_i - p_0 / \sqrt{N_i^{\text{pe}} - p_1 - p_2 / N_i^{\text{pe}}} \quad (2.6)$$

461     The parameters  $(p_0, p_1, p_2)$  were optimized to (9.42, 0.74, -4.60) for Hamamatsu PMTs and (41.31,  
462     -12.04, -20.02) for NNVT PMTs [35]. The results presented in figure 2.13b shows that the time based  
463     algorithm provide a more accurate vertex and is unbiased even in the TR area. This results  $(\vec{r}_0, t_0)$  is  
464     used as initial value for the likelihood algorithm.

#### 465 Time likelihood algorithm

466     The time likelihood algorithm use the residual time expressed as follow

$$t_{\text{res}}^i(\vec{r}_0, t_0) = t_i - \text{tof}_i - t_0 \quad (2.7)$$

467     In a first order approximation, the scintillator time response Probability Density Function (PDF)  
468     can be described as the emission time profile of the scintillation photons, the Time Transit Spread  
469     (TTS) and the dark noise of the PMTs. The emission time profile  $f(t_{\text{res}})$  is described like

$$f(t_{\text{res}}) = \sum_k \frac{\rho_k}{\tau_k} e^{-\frac{t_{\text{res}}}{\tau_k}}, \sum_k \rho_k = 1 \quad (2.8)$$

470     as the sum of the  $k$  component that emit light in the LS each one characterised by it's decay time  $\tau_k$   
471     and intensity fraction  $\rho_k$ . The TTS component is expressed as a gaussian convolution

$$g(t_{\text{res}}) = \frac{1}{\sqrt{2\pi}\sigma} e^{-\frac{(t_{\text{res}}-\nu)^2}{2\sigma^2}} \cdot f(t_{\text{res}}) \quad (2.9)$$

472 where  $\sigma$  is the TTS of PMTs and  $\nu$  is the average transit time. The dark noise is not correlated with any  
 473 physical events and considered as constant rate over the time window considered  $T$ . By normalizing  
 474 the dark noise probability  $\epsilon(t_{\text{res}})$  as  $\int_T \epsilon(t_{\text{res}}) dt_{\text{res}} = \epsilon_{\text{dn}}$ , it can be integrated in the PDF as

$$p(t_{\text{res}}) = (1 - \epsilon_{\text{dn}}) \cdot g(t_{\text{res}}) + \epsilon(t_{\text{res}}) \quad (2.10)$$

475 The distribution of the residual time  $t_{\text{res}}$  of an event can then be compared to  $p(t_{\text{res}})$  and the best  
 476 fitting vertex  $\vec{r}_0$  and  $t_0$  can be chosen by minimizing

$$\mathcal{L}(\vec{r}_0, t_0) = -\ln \left( \prod_i p(t_{\text{res}}^i) \right) \quad (2.11)$$

477 The parameter of Eq. 2.10 can be measured experimentally. The results shown in figure 2.14  
 478 used PDF from monte carlo simulation. The results shows that  $R_{\text{rec}} - R_{\text{true}}$  is biased depending  
 479 on the energy. While this could be corrected using calibration, another algorithm based on charge  
 480 likelihood was developed to correct this problem.

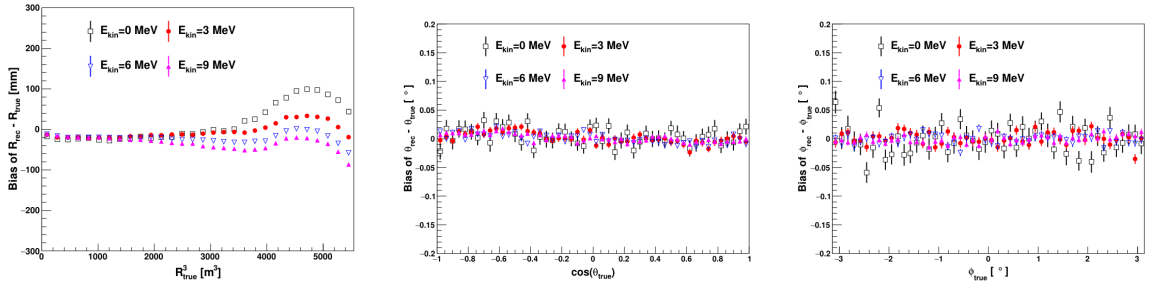


FIGURE 2.14 – Bias of the reconstructed radius  $R$  (left),  $\theta$  (middle) and  $\phi$  (right) for multiple energies by the time likelihood algorithm

#### 481 Charge likelihood algorithm

482 Similarly to the time likelihood algorithms that use a timing PDF, the charge likelihood algorithm  
 483 use a PE PDF for each PMT depending on the energy and position of the event. With  $\mu(\vec{r}_0, E)$  the  
 484 mean expected number of PE detected by each PMT, the probability to observe  $N_{pe}$  in a PMT follow  
 485 a Poisson distribution. Thus

- 486 — The probability to observe no hit ( $N_{pe} = 0$ ) in the  $j$ th PMT is  $P_{\text{nohit}}^j(\vec{r}_0, E) = e^{-\mu_j}$
- 487 — The probability to observe  $N_{pe} \neq 0$  in the  $i$ th PMT is  $P_{\text{hit}}^i(\vec{r}_0, E) = \frac{\mu^{N_{pe}} e^{-\mu_i}}{N_{pe}^i!}$

488 Therefore, the probability to observe a specific hit pattern can be expressed as

$$P(\vec{r}_0, E) = \prod_j P_{\text{nohit}}^j(\vec{r}_0, E) \cdot \prod_i P_{\text{hit}}^i(\vec{r}_0, E) \quad (2.12)$$

489 The best fit values of  $\vec{R}_0$  and  $E$  can then be calculated by minimizing the negative log-likelihood

$$\mathcal{L}(\vec{r}_0, E) = -\ln(P(\vec{r}_0, E)) \quad (2.13)$$

490 In principle,  $\mu_i(\vec{r}_0, E)$  could be expressed

$$\mu_i(\vec{r}_0, E) = Y \cdot \frac{\Omega(\vec{r}_0, r_i)}{4\pi} \cdot \epsilon_i \cdot f(\theta_i) \cdot e^{-\sum_m \frac{d_m}{\zeta_m}} \cdot E + \delta_i \quad (2.14)$$

491 where  $Y$  is the energy scale factor,  $\Omega(\vec{r}_0, r_i)$  is the solid angle of the  $i$ th PMT,  $\epsilon_i$  is its detection

efficiency,  $f(\theta_i)$  its angular response,  $\zeta_m$  is the attenuation length in the materials and  $\delta_i$  the expected number of dark noise.

However Eq. 2.14 assume that the scintillation light yield is linear with energy and describe poorly the contribution of indirect light, shadow effect due to the supporting structure and the total reflection effects. The solution is to use data driven methods to produce the pdf by using the calibrations sources and position described in section 2.3. In the results presented in figures 2.15, the PDF was produced using MC simulation and 29 specific calibrations position [35] along the Z-axis of the detector. We see that the charge likelihood algorithm show little bias in the TR area and a

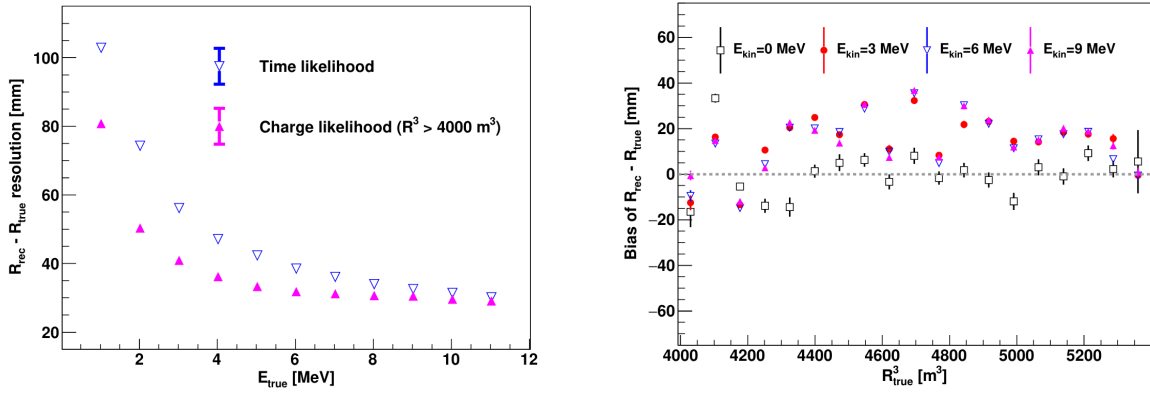


FIGURE 2.15 – On the left: Resolution of the reconstructed  $R$  as a function of the energy in the TR area ( $R^3 > 4000 \text{ m}^3 \equiv R > 16 \text{ m}$ ) by the charge and time likelihood algorithms. On the right: Bias of the reconstructed  $R$  in the TR area for different energies by the charge likelihood algorithm

better resolution than the time likelihood. The figure 2.16 shows the radial resolution of the different algorithm presented for this section, we can see the refinement at each step and that the charge likelihood yield the best results.

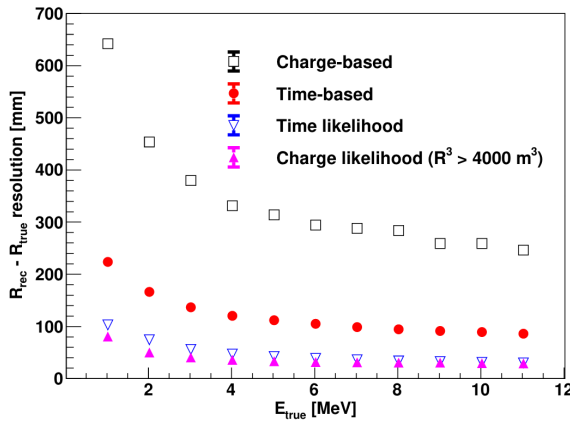


FIGURE 2.16 – Radial resolution of the different vertex reconstruction algorithms as a function of the energy

The charge based likelihood algorithms already give some information on the energy as Eq. 2.13 is minimized but the energy can be further refined as shown in the next section.

### 505 2.6.2 Energy reconstruction

506 As explained in section 2.1.1, energy resolution is crucial for the NMO and oscillation parameters  
 507 measurements. Thus the energy reconstruction algorithm should take into consideration as much  
 508 detector effect as possible. The following method is a data driven method based on calibration  
 509 samples inspired by the charge likelihood algorithm described above [39].

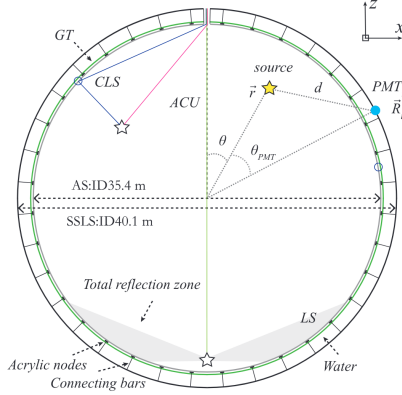


FIGURE 2.17 – Definition of the variables used in the energy reconstruction

#### 510 Charge estimation

511 The most important element in the energy reconstruction is  $\mu_i(\vec{r}_0, E)$  described in Eq. 2.14. For  
 512 realistic cases, we also need to take into account the electronics effect that were omitted in the  
 513 previous section. Those effect will cause a charge smearing due to the uncertainties in the  $N_{pe}$   
 514 reconstruction. Thus we define  $\hat{\mu}^L(\vec{r}_0, E)$  which is the expected  $N_{pe}/E$  in the whole detector for an  
 515 event with visible energy  $E_{vis}$  and position  $\vec{r}_0$ . The position of the event and PMTs are now defined  
 516 using  $(r, \theta, \theta_{pmt})$  as defined in figure 2.17.

$$\hat{\mu}(r, \theta, \theta_{pmt}, E_{vis}) = \frac{1}{E_{vis}} \frac{1}{M} \sum_i^M \frac{\bar{q}_i - \mu_i^D}{\text{DE}_i}, \quad \mu_i^D = \text{DNR}_i \cdot L \quad (2.15)$$

517 where  $i$  runs over the PMTs with the same  $\theta_{pmt}$ ,  $\text{DE}_i$  is the detection efficiency of the  $i$ th PMT.  $\mu_i^D$   
 518 is the expected number of dark noise photoelectrons in the time window  $L$ . The time window have  
 519 been optimized to  $L = 280$  ns [39].  $\bar{q}_i$  is the average recorded photoelectrons in the time window  
 520 and  $\bar{Q}_i$  is the expected average charge for 1 photoelectron. The  $N_{pe}$  map is constructed following the  
 521 procedure described in [34].

#### 522 Time estimation

523 The second important observable is the hit time of photons that was previously defined in Eq.  
 524 2.7. It is here refined as

$$t_r = t_h - \text{tof} - t_0 = t_{LS} + t_{TT} \quad (2.16)$$

525 where  $t_h$  is the time of hit,  $t_{LS}$  is the scintillation time and  $t_{TT}$  the transit time of PMTs that is described  
 526 by a gaussian

$$t_{TT} = \mathcal{N}(\mu_{TT} + t_d, \sigma_{TT}) \quad (2.17)$$

527 where  $\mu_{TT}$  is the mean transit time in PMTs,  $\sigma_{TT}$  is the Transit Time Spread (TTS) of the PMTs and  $t_d$   
 528 is the delay time in the electronics. The effective refraction index of the LS is also corrected to take

529 into account the propagation distance in the detector.

530 The timing PDF  $P_T(t_r|r, d, \mu_l, \mu_d, k)$  can now be generated using calibration sources [39]. This PDF  
 531 describe the probability that the residual time of the first photon hit is in  $[t_r, t_r + \delta]$  with  $r$  the radius  
 532 of the event vertex,  $d = |\vec{r} - \vec{r}_{PMT}|$  the propagation distance,  $\mu_l$  and  $\mu_d$  the expected number of PE  
 533 and dark noise in the electronic reading window and  $k$  is the detected number of PE.

534 Now let denote  $f(t, r, d)$  the probability density function of "photoelectron hit a time t" for an  
 535 event happening at  $r$  where the photons traveled the distance  $d$  in the LS

$$F(t, r, d) = \int_t^L f(t', r, d) dt' \quad (2.18)$$

536 Based on the PDF for one photon  $k = 1$ , one can define

$$P_T^l(t|k = n) = I_n^l[f_l(t)F_l^{n-1}(t)] \quad (2.19)$$

537 where the indicator  $l$  means that the photons comes from the LS and  $I_n^l$  a normalisation factor. To this  
 538 pdf we add the probability to have photons coming from the dark noise indicated by the indicator  $d$   
 539 using

$$f_d(t) = 1/L, F_d(t) = 1 - \frac{t}{L} \quad (2.20)$$

540 and so for the case where only one photon is detected by the PMT ( $k = 1$ )

$$P_T(t|\mu_l, \mu_d, k = 1) = I_1[P(1, \mu_l)P(0, \mu_d)f_l(t) + P(0, \mu_l)P(1, \mu_d)f_d(t)] \quad (2.21)$$

541 where  $P(k_\alpha, \mu_\alpha)$  is the Poisson probability to detect  $k_\alpha$  PE from  $\alpha \in \{l, d\}$  with the condition  $k_l + k_d =$   
 542  $k$ .

543 Now that we have the individual timing and charge probability we can construct the charge  
 544 likelihood referred as QMLE:

$$\mathcal{L}(q_1, q_2, \dots, q_N | \vec{r}, E_{vis}) = \prod_{j \in \text{unfired}} e^{-\mu_j} \prod_{i \in \text{fired}} \left( \sum_{k=1}^K P_Q(q_i|k) \cdot P(k, \mu_i) \right) \quad (2.22)$$

545 where  $\mu_i = E_{vis}\hat{\mu}_i^L + \mu_i^D$  and  $P(k, \mu_i)$  is the Poisson probability of observing  $k$  PE.  $P_Q(q_i|k)$  is the  
 546 charge pdf for  $k$  PE. And we can also construct the time likelihood referred as TMLE:

$$\mathcal{L}(t_{1,r}, t_{2,r}, \dots, t_{N,r} | \vec{r}, t_0) = \prod_{i \in \text{hit}} \frac{\sum_{k=1}^K P_T(t_{i,r}|r, d, \mu_i^l, \mu_i^d, k) \cdot P(k, \mu_i^l + \mu_i^d)}{\sum_{k=1}^K P(k, \mu_i^l + \mu_i^d)} \quad (2.23)$$

547 where  $K$  is cut to 20 PE and hit is the set of hits satisfying  $-100 < t_{i,r} < 500$  ns.

548 Merging those two likelihood give the charge-time likelihood QTMLLE

$$\mathcal{L}(q_1, q_2, \dots, q_N; t_{1,r}, t_{2,r}, \dots, t_{N,r} | \vec{r}, t_0, E_{vis}) = \mathcal{L}(q_1, q_2, \dots, q_N | \vec{r}, E_{vis}) \cdot \mathcal{L}(t_{1,r}, t_{2,r}, \dots, t_{N,r} | \vec{r}, t_0) \quad (2.24)$$

549 The radial and energy resolutions of the different likelihood are presented in figure 2.18 (from  
 550 [39]). We can see the improvement of adding the time information to the vertex reconstruction and  
 551 that an increase in vertex precision can bring improvement in the energy resolution, especially at low  
 552 energies.

553 Data driven methods prove to be performant in the energy and vertex reconstruction given that  
 554 we have enough calibrations sources to produce the PDF. In the next section, we'll see another type  
 555 of data-driven method based on machine learning.

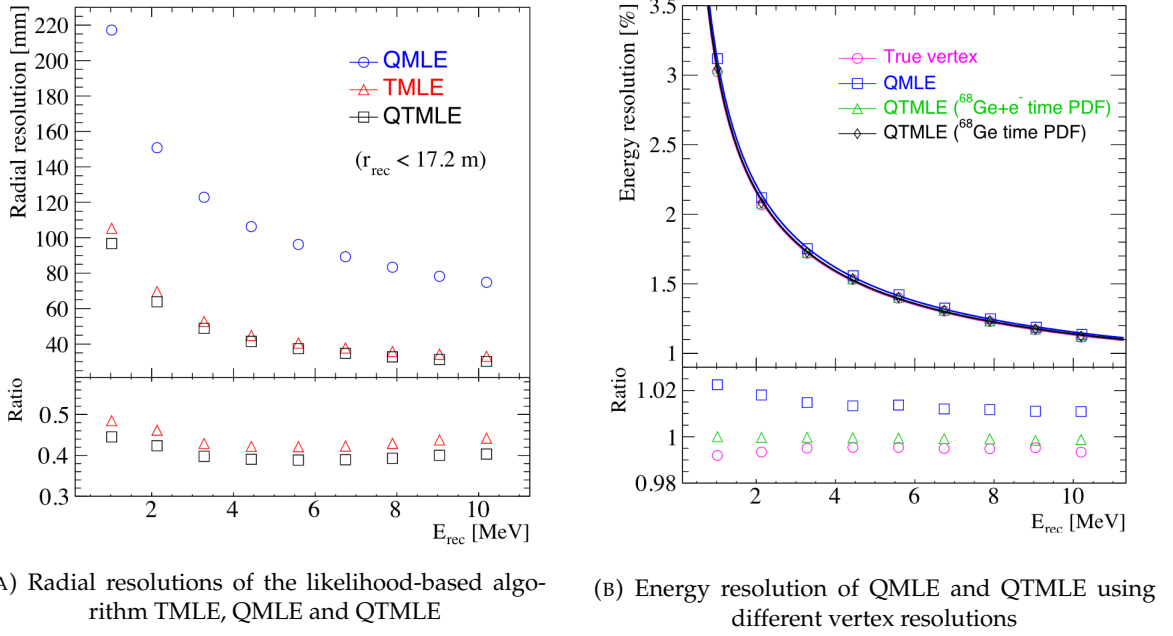


FIGURE 2.18

### 2.6.3 Machine learning for reconstruction

Machine learning (ML) is a family of data-driven algorithms that are inferring behavior and results from a training dataset. A overview of methods and detailed explanation of the Neural Network (NN) subfamily can be found in Chapter 3.

The power of ML is the ability to model complex response to a specific problem. In JUNO the reconstruction problematic can be expressed as follow: knowing that each PMT, large or small, detected a given number of PE  $Q$  at a given time  $t$  and their position is  $x, y, z$  where did the energy was deposited and how much energy was it, modeling a function that naively goes:

$$\mathbb{R}^{5 \times N_{pmt}} \mapsto \mathbb{R}^4 \quad (2.25)$$

It is worth pointing that while this is already a lot in informations, this is not the rawest representation of the experiment. We could indeed replace the charge and time by the waveform in the time window of the event but that would lead to an input representation size that would exceed our computational limits. Also, due to those computational limits, most of the ML algorithm reduce this input phase space either by structurally encoding the information (pictures, graph), by aggregating it (mean, variance, ...) or by exploiting invariance and equivariance of the experiment (rotational invariance due to the sphericity, ...).

For machine learning to converge to performant algorithm, a large dataset exploring all the phase space of interest is needed. For the following studies, data from the monte carlo simulation presented in section 2.5 are used for training. When the detector will be finished calibrations sources will be complementarily be used.

#### Boosted Decision Tree (BDT)

On of the most classic ML method used in physics in last years is the Boosted Decision Tree (see chapter 3.2). They have been explored for vertex reconstruction [40] et for energy reconstruction [40, 41].

579 For vertex and energy reconstruction a BDT was developed using the aggregated informations  
 580 presented in 2.6.

Parameter	description
$nHits$	Total number of hits
$x_{cc}, y_{cc}, z_{cc}, R_{cc}$	Coordinates of the center of charge
$ht_{mean}, ht_{std}$	Hit time mean and standard deviation

TABLE 2.6 – Features used by the BDT for vertex reconstruction

581 Its reconstruction performances are presented in figure 2.20.

582 A second and more advanced BDT, subsequently named BDTE, that only reconstruct energy use  
 583 a different set of features [41]. They are presented in the table 2.7

#### 584 Neural Network (NN)

585 The physics have shown a rising for Neural Network (NN) in the past years for event reconstruc-  
 586 tion, notably in the neutrino community [42–45]. Three type of neural networks have explored for  
 587 event reconstruction in JUNO Deep Neural Network (DNN), Convolutional Neural Network (CNN)  
 588 and Graph Network (GNN). More explanation about those neural network can be found in chapter  
 589 3.

590 The CNN are using 2D projection of the detector representing it as an image with two channel,  
 591 one for the charge  $Q$  and one for the time  $t$ . The position of the PMTs is structurally encoded in the  
 592 pixel containing the information of this PMT. In [40], the pixel is chosen based on a transformation  
 593 of  $\theta$  and  $\phi$  coordinates to the 2D plane and rounded to the nearest pixel. A sufficiently large image  
 594 has been chosen to prevent two PMT to be located in the same pixel. An example of this projection  
 595 can be found in figure 2.19. The performances of the CNN can be found in figure 2.20.

596 Using 2D have the upside of encoding a large part of the informations structurally but loose  
 597 the rotational invariance of the detector. It also give undefined information to the neural network  
 598 (what is a pixel without PMT ? What should be its charge and time ?), cause deformation in the  
 599 representation of the detector (sides of projection) and loose topological informations.

600 One of the way to present structurally the sphericity of JUNO to a NN is to use a graph: A  
 601 collection of objects  $V$  called nodes and relations  $E$  called edges, each relation associated to a couple  
 602  $v_1, v_2$  forming the graph  $G(E, V)$ . Nodes and edges can hold informations or features. In [40] the  
 603 nodes, are geometrical region of the detector as defined by the HealPix [46]. The features of the nodes  
 604 are aggregated informations from the PMTs it contains. The edges contains geographic informations  
 605 of the nodes relative positions.

606 This data representation has the advantages to keep the topology of the detector intact. It also  
 607 permit the use of rotational invariant algorithms for the NN, thus taking advantage of the symmetries  
 608 of the detector.

AccumCharge	$ht_{5\%-2\%}$
$R_{cht}$	$pe_{mean}$
$z_{cc}$	$J_{cht}$
$pe_{std}$	$\phi_{cc}$
nPMTs	$ht_{35\%-30\%}$
$ht_{kurtosis}$	$ht_{20\%-15\%}$
$ht_{25\%-20\%}$	$pe_{35\%}$
$R_{cc}$	$ht_{30\%-25\%}$

TABLE 2.7 – Features used by the BDTE algorithm.  $pe$  and  $ht$  reference the charge  
 and hit-time distribution respectively and the percentages are the quantiles of those  
 distributions.  $cht$  and  $cc$  reference the barycenters of hit time and charge respectively

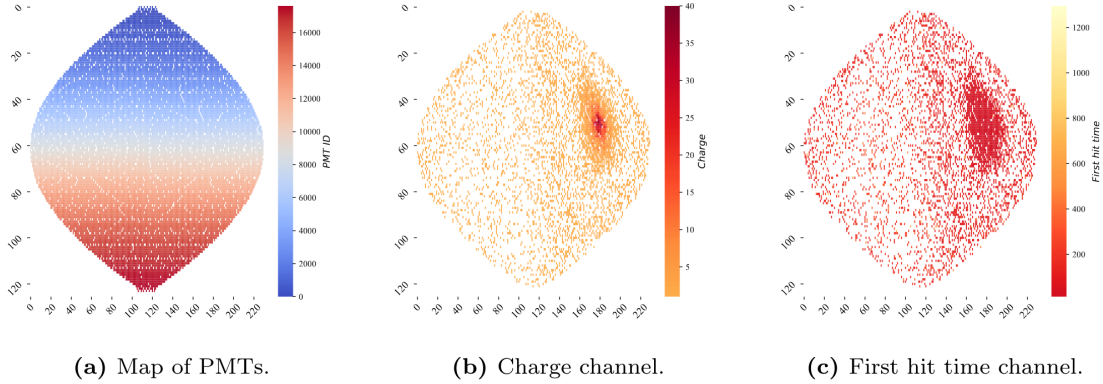


FIGURE 2.19 – Projection of the LPMTs in JUNO on a 2D plane. (a) Show the distribution of all PMTs and (b) and (c) are example of what the charge and time channel looks like respectively

609 The neural network then process the graph using Chebyshev Convolutions [47]. The performances of the GNN are presented in figure 2.20.  
 610

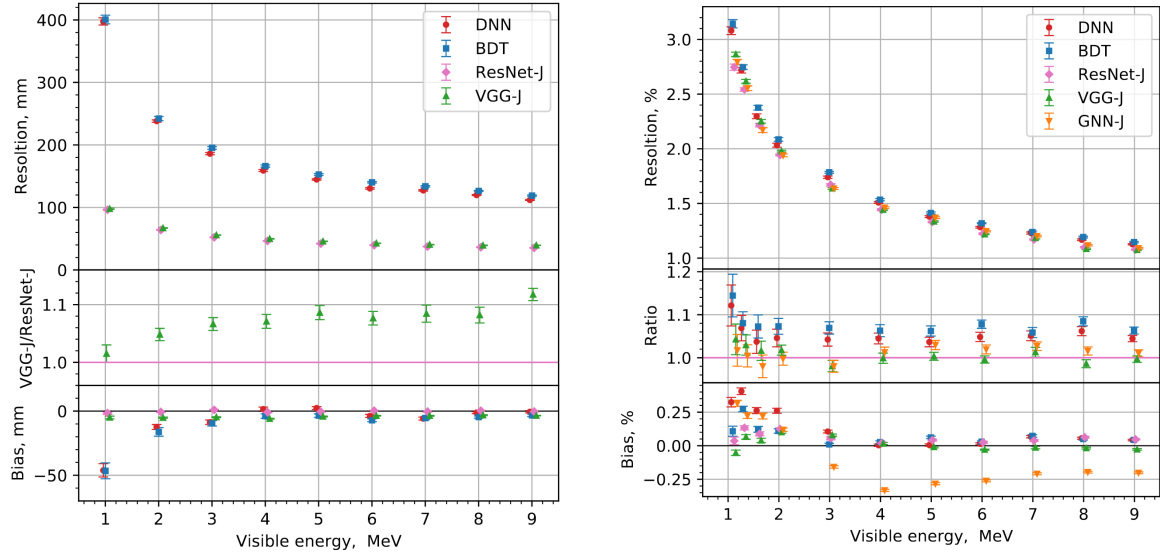


FIGURE 2.20 – Radial (left) and energy (right) resolutions of different ML algorithms. The results presented here are from [40]. DNN is a deep neural network, BDT is a BDT, ResNet-J and VGG-J are CNN and GNN-J is a GNN.

611 Overall ML algorithms show similar performances as classical algorithms in term of energy  
 612 reconstructions with the more complex structure CNN and GNN showing better performances than  
 613 BDT and DNN. For vertex reconstruction, the BDT and DNN show poor performance while CNN  
 614 are on the level of the classical algorithms.

## 615 2.7 JUNO sensitivity to NMO and precise measurements

616 Once the event is reconstructed, and the energy spectrum is produced, we will need to extract the  
 617 NMO oscillation parameters from it.

---

**6<sub>18</sub> 2.7.1 Fitting procedure**

<sub>619</sub> **Chapter 3**

<sub>620</sub> **Machine learning and Artificial  
Neural Network**

<sub>622</sub> **3.1 History of the Machine learning**

<sub>623</sub> **3.2 Boosted Decision Tree (BDT)**

<sub>624</sub> **3.3 Artificial Neural Network (NN)**

<sub>625</sub> **3.3.1 Fully Connected Deep Neural Network (FCDNN)**

<sub>626</sub> **3.3.2 Convolutional Neural Network (CNN)**

<sub>627</sub> **3.3.3 Graph Neural Network (GNN)**

<sub>628</sub> **3.3.4 Adversarial Neural Network (ANN)**

<sub>629</sub> **Generative Adversarial Network (GAN)**

<sub>630</sub> **Reinforcement Learning (RL)**

<sub>631</sub> **Random Search (RS)**

<sub>632</sub> **Bayesian Optimization**



<sup>633</sup> **Chapter 4**

<sup>634</sup> **Image recognition for IBD  
reconstruction with the SPMT system**

<sup>635</sup>



<sup>636</sup> **Chapter 5**

<sup>637</sup> **Graph representation of JUNO for IBD  
reconstruction with the LPMT system**

<sup>638</sup>



<sup>639</sup> Chapter 6

<sup>640</sup> **Reliability of machine learning  
methods**

<sup>641</sup>



<sup>642</sup> Chapter 7

<sup>643</sup> **Discrimination of e+/e- events in  
JUNO**

<sup>644</sup>



<sup>645</sup> **Chapter 8**

<sup>646</sup> **Conclusion**



# Bibliography

- [1] Liang Zhan, Yifang Wang, Jun Cao, and Liangjian Wen. "Determination of the Neutrino Mass Hierarchy at an Intermediate Baseline". *Physical Review D* 78.11 (Dec. 10, 2008), 111103. ISSN: 1550-7998, 1550-2368. DOI: [10 . 1103 / PhysRevD . 78 . 111103](https://doi.org/10.1103/PhysRevD.78.111103). eprint: [0807 . 3203 \[hep-ex, physics:hep-ph\]](https://arxiv.org/abs/0807.3203). URL: [http://arxiv.org/abs/0807.3203](https://arxiv.org/abs/0807.3203) (visited on 09/18/2023).
- [2] Fengpeng An et al. "Neutrino Physics with JUNO". *Journal of Physics G: Nuclear and Particle Physics* 43.3 (Mar. 1, 2016), 030401. ISSN: 0954-3899, 1361-6471. DOI: [10 . 1088 / 0954 - 3899 / 43 / 3 / 030401](https://doi.org/10.1088/0954-3899/43/3/030401). eprint: [1507 . 05613 \[hep-ex, physics:physics\]](https://arxiv.org/abs/1507.05613). URL: [http://arxiv.org/abs/1507.05613](https://arxiv.org/abs/1507.05613) (visited on 07/28/2023).
- [3] Liang Zhan, Yifang Wang, Jun Cao, and Liangjian Wen. "Experimental Requirements to Determine the Neutrino Mass Hierarchy Using Reactor Neutrinos". *Physical Review D* 79.7 (Apr. 14, 2009), 073007. ISSN: 1550-7998, 1550-2368. DOI: [10 . 1103 / PhysRevD . 79 . 073007](https://doi.org/10.1103/PhysRevD.79.073007). eprint: [0901 . 2976 \[hep-ex\]](https://arxiv.org/abs/0901.2976). URL: [http://arxiv.org/abs/0901.2976](https://arxiv.org/abs/0901.2976) (visited on 09/18/2023).
- [4] A. A. Hahn, K. Schreckenbach, W. Gelletly, F. von Feilitzsch, G. Colvin, and B. Krusche. "Antineutrino spectra from 241Pu and 239Pu thermal neutron fission products". *Physics Letters B* 218.3 (Feb. 23, 1989), 365–368. ISSN: 0370-2693. DOI: [10 . 1016 / 0370 - 2693 \(89\) 91598 - 0](https://doi.org/10.1016/0370-2693(89)91598-0). URL: <https://www.sciencedirect.com/science/article/pii/0370269389915980> (visited on 01/16/2024).
- [5] Th A. Mueller et al. "Improved Predictions of Reactor Antineutrino Spectra". *Physical Review C* 83.5 (May 23, 2011), 054615. ISSN: 0556-2813, 1089-490X. DOI: [10 . 1103 / PhysRevC . 83 . 054615](https://doi.org/10.1103/PhysRevC.83.054615). eprint: [1101 . 2663 \[hep-ex, physics:nucl-ex\]](https://arxiv.org/abs/1101.2663). URL: [http://arxiv.org/abs/1101.2663](https://arxiv.org/abs/1101.2663) (visited on 01/16/2024).
- [6] F. von Feilitzsch, A. A. Hahn, and K. Schreckenbach. "Experimental beta-spectra from 239Pu and 235U thermal neutron fission products and their correlated antineutrino spectra". *Physics Letters B* 118.1 (Dec. 2, 1982), 162–166. ISSN: 0370-2693. DOI: [10 . 1016 / 0370 - 2693 \(82\) 90622 - 0](https://doi.org/10.1016/0370-2693(82)90622-0). URL: <https://www.sciencedirect.com/science/article/pii/0370269382906220> (visited on 01/16/2024).
- [7] K. Schreckenbach, G. Colvin, W. Gelletly, and F. Von Feilitzsch. "Determination of the antineutrino spectrum from 235U thermal neutron fission products up to 9.5 MeV". *Physics Letters B* 160.4 (Oct. 10, 1985), 325–330. ISSN: 0370-2693. DOI: [10 . 1016 / 0370 - 2693 \(85\) 91337 - 1](https://doi.org/10.1016/0370-2693(85)91337-1). URL: <https://www.sciencedirect.com/science/article/pii/0370269385913371> (visited on 01/16/2024).
- [8] Patrick Huber. "On the determination of anti-neutrino spectra from nuclear reactors". *Physical Review C* 84.2 (Aug. 29, 2011), 024617. ISSN: 0556-2813, 1089-490X. DOI: [10 . 1103 / PhysRevC . 84 . 024617](https://doi.org/10.1103/PhysRevC.84.024617). eprint: [1106 . 0687 \[hep-ex, physics:hep-ph, physics:nucl-ex, physics:nucl-th\]](https://arxiv.org/abs/1106.0687). URL: [http://arxiv.org/abs/1106.0687](https://arxiv.org/abs/1106.0687) (visited on 01/16/2024).
- [9] P. Vogel, G. K. Schenter, F. M. Mann, and R. E. Schenter. "Reactor antineutrino spectra and their application to antineutrino-induced reactions. II". *Physical Review C* 24.4 (Oct. 1, 1981). Publisher: American Physical Society, 1543–1553. DOI: [10 . 1103 / PhysRevC . 24 . 1543](https://doi.org/10.1103/PhysRevC.24.1543). URL: <https://link.aps.org/doi/10.1103/PhysRevC.24.1543> (visited on 01/16/2024).

- [10] D. A. Dwyer and T. J. Langford. "Spectral Structure of Electron Antineutrinos from Nuclear Reactors". *Physical Review Letters* 114.1 (Jan. 7, 2015), 012502. ISSN: 0031-9007, 1079-7114. DOI: [10.1103/PhysRevLett.114.012502](https://doi.org/10.1103/PhysRevLett.114.012502). eprint: [1407.1281\[hep-ex, physics:nucl-ex\]](https://arxiv.org/abs/1407.1281). URL: <http://arxiv.org/abs/1407.1281> (visited on 01/16/2024).
- [11] JUNO Collaboration et al. "Sub-percent Precision Measurement of Neutrino Oscillation Parameters with JUNO". *Chinese Physics C* 46.12 (Dec. 1, 2022), 123001. ISSN: 1674-1137, 2058-6132. DOI: [10.1088/1674-1137/ac8bc9](https://doi.org/10.1088/1674-1137/ac8bc9). eprint: [2204.13249\[hep-ex\]](https://arxiv.org/abs/2204.13249). URL: <http://arxiv.org/abs/2204.13249> (visited on 08/11/2023).
- [12] JUNO Collaboration et al. *TAO Conceptual Design Report: A Precision Measurement of the Reactor Antineutrino Spectrum with Sub-percent Energy Resolution*. May 18, 2020. DOI: [10.48550/arXiv.2005.08745](https://doi.org/10.48550/arXiv.2005.08745). eprint: [2005.08745\[hep-ex, physics:nucl-ex, physics:physics\]](https://arxiv.org/abs/2005.08745). URL: <http://arxiv.org/abs/2005.08745> (visited on 01/18/2024).
- [13] G. Mention, M. Fechner, Th. Lasserre, Th. A. Mueller, D. Lhuillier, M. Cribier, and A. Letourneau. "Reactor antineutrino anomaly". *Physical Review D* 83.7 (Apr. 29, 2011). Publisher: American Physical Society, 073006. DOI: [10.1103/PhysRevD.83.073006](https://doi.org/10.1103/PhysRevD.83.073006). URL: <https://link.aps.org/doi/10.1103/PhysRevD.83.073006> (visited on 03/05/2024).
- [14] V. Kopeikin, M. Skorokhvatov, and O. Titov. "Reevaluating reactor antineutrino spectra with new measurements of the ratio between  $^{235}\text{U}$  and  $^{239}\text{Pu}$   $\beta^-$  spectra". *Physical Review D* 104.7 (Oct. 25, 2021), L071301. ISSN: 2470-0010, 2470-0029. DOI: [10.1103/PhysRevD.104.L071301](https://doi.org/10.1103/PhysRevD.104.L071301). eprint: [2103.01684\[hep-ph, physics:nucl-ex, physics:nucl-th\]](https://arxiv.org/abs/2103.01684). URL: <http://arxiv.org/abs/2103.01684> (visited on 01/18/2024).
- [15] A. Letourneau et al. "On the origin of the reactor antineutrino anomalies in light of a new summation model with parameterized  $\beta^-$  transitions". *Physical Review Letters* 130.2 (Jan. 10, 2023), 021801. ISSN: 0031-9007, 1079-7114. DOI: [10.1103/PhysRevLett.130.021801](https://doi.org/10.1103/PhysRevLett.130.021801). eprint: [2205.14954\[hep-ex, physics:hep-ph\]](https://arxiv.org/abs/2205.14954). URL: <http://arxiv.org/abs/2205.14954> (visited on 01/16/2024).
- [16] Particle Data Group et al. "Review of Particle Physics". *Progress of Theoretical and Experimental Physics* 2020.8 (Aug. 14, 2020), 083C01. ISSN: 2050-3911. DOI: [10.1093/ptep/ptaa104](https://doi.org/10.1093/ptep/ptaa104). URL: <https://doi.org/10.1093/ptep/ptaa104> (visited on 12/04/2023).
- [17] Super-Kamiokande Collaboration et al. "Diffuse Supernova Neutrino Background Search at Super-Kamiokande". *Physical Review D* 104.12 (Dec. 10, 2021), 122002. ISSN: 2470-0010, 2470-0029. DOI: [10.1103/PhysRevD.104.122002](https://doi.org/10.1103/PhysRevD.104.122002). eprint: [2109.11174\[astro-ph, physics:hep-ex\]](https://arxiv.org/abs/2109.11174). URL: <http://arxiv.org/abs/2109.11174> (visited on 02/28/2024).
- [18] Alessandro Strumia and Francesco Vissani. "Precise quasielastic neutrino/nucleon cross section". *Physics Letters B* 564.1 (July 2003), 42–54. ISSN: 03702693. DOI: [10.1016/S0370-2693\(03\)00616-6](https://doi.org/10.1016/S0370-2693(03)00616-6). eprint: [astro-ph/0302055](https://arxiv.org/abs/astro-ph/0302055). URL: <http://arxiv.org/abs/astro-ph/0302055> (visited on 01/16/2024).
- [19] Daya Bay et al. *Optimization of the JUNO liquid scintillator composition using a Daya Bay antineutrino detector*. July 1, 2020. DOI: [10.48550/arXiv.2007.00314](https://doi.org/10.48550/arXiv.2007.00314). eprint: [2007.00314\[hep-ex, physics:physics\]](https://arxiv.org/abs/2007.00314). URL: <http://arxiv.org/abs/2007.00314> (visited on 07/26/2023).
- [20] J. B. Birks. "CHAPTER 3 - THE SCINTILLATION PROCESS IN ORGANIC MATERIALS—I". *The Theory and Practice of Scintillation Counting*. Ed. by J. B. Birks. International Series of Monographs in Electronics and Instrumentation. Jan. 1, 1964, 39–67. ISBN: 978-0-08-010472-0. DOI: [10.1016/B978-0-08-010472-0.50008-2](https://doi.org/10.1016/B978-0-08-010472-0.50008-2). URL: <https://www.sciencedirect.com/science/article/pii/B9780080104720500082> (visited on 02/07/2024).
- [21] Photomultiplier tube R12860 | Hamamatsu Photonics. URL: [https://www.hamamatsu.com/eu/en/product/optical-sensors/pmt/pmt\\_tube-alone/head-on-type/R12860.html](https://www.hamamatsu.com/eu/en/product/optical-sensors/pmt/pmt_tube-alone/head-on-type/R12860.html) (visited on 02/08/2024).

- [22] Yan Zhang, Ze-Yuan Yu, Xin-Ying Li, Zi-Yan Deng, and Liang-Jian Wen. "A complete optical model for liquid-scintillator detectors". *Nuclear Instruments and Methods in Physics Research Section A: Accelerators, Spectrometers, Detectors and Associated Equipment* 967 (July 2020), 163860. ISSN: 01689002. DOI: [10.1016/j.nima.2020.163860](https://doi.org/10.1016/j.nima.2020.163860). eprint: [2003.12212\[physics\]](https://arxiv.org/abs/2003.12212). URL: <http://arxiv.org/abs/2003.12212> (visited on 02/07/2024).
- [23] Hai-Bo Yang et al. "Light Attenuation Length of High Quality Linear Alkyl Benzene as Liquid Scintillator Solvent for the JUNO Experiment". *Journal of Instrumentation* 12.11 (Nov. 27, 2017), T11004–T11004. ISSN: 1748-0221. DOI: [10.1088/1748-0221/12/11/T11004](https://doi.org/10.1088/1748-0221/12/11/T11004). eprint: [1703.01867\[hep-ex, physics:physics\]](https://arxiv.org/abs/1703.01867). URL: <http://arxiv.org/abs/1703.01867> (visited on 07/28/2023).
- [24] JUNO Collaboration et al. *The Design and Sensitivity of JUNO's scintillator radiopurity pre-detector OSIRIS*. Mar. 31, 2021. DOI: [10.48550/arXiv.2103.16900](https://doi.org/10.48550/arXiv.2103.16900). eprint: [2103.16900\[physics\]](https://arxiv.org/abs/2103.16900). URL: <http://arxiv.org/abs/2103.16900> (visited on 02/07/2024).
- [25] Angel Abusleme et al. "Mass Testing and Characterization of 20-inch PMTs for JUNO". *The European Physical Journal C* 82.12 (Dec. 24, 2022), 1168. ISSN: 1434-6052. DOI: [10.1140/epjc/s10052-022-11002-8](https://doi.org/10.1140/epjc/s10052-022-11002-8). eprint: [2205.08629\[hep-ex, physics:physics\]](https://arxiv.org/abs/2205.08629). URL: <http://arxiv.org/abs/2205.08629> (visited on 02/08/2024).
- [26] Yang Han. "Dual Calorimetry for High Precision Neutrino Oscillation Measurement at JUNO Experiment". AstroParticule et Cosmologie, France, Paris U. VII, APC, June 2021.
- [27] R. Acquaferda et al. "The OPERA experiment in the CERN to Gran Sasso neutrino beam". *Journal of Instrumentation* 4.4 (Apr. 2009), P04018. ISSN: 1748-0221. DOI: [10.1088/1748-0221/4/04/P04018](https://doi.org/10.1088/1748-0221/4/04/P04018). URL: <https://dx.doi.org/10.1088/1748-0221/4/04/P04018> (visited on 02/29/2024).
- [28] JUNO collaboration et al. "Calibration Strategy of the JUNO Experiment". *Journal of High Energy Physics* 2021.3 (Mar. 2021), 4. ISSN: 1029-8479. DOI: [10.1007/JHEP03\(2021\)004](https://doi.org/10.1007/JHEP03(2021)004). eprint: [2011.06405\[hep-ex, physics:physics\]](https://arxiv.org/abs/2011.06405). URL: <http://arxiv.org/abs/2011.06405> (visited on 08/10/2023).
- [29] Tao Lin et al. "The Application of SNiPER to the JUNO Simulation". *Journal of Physics: Conference Series* 898.4 (Oct. 2017). Publisher: IOP Publishing, 042029. ISSN: 1742-6596. DOI: [10.1088/1742-6596/898/4/042029](https://doi.org/10.1088/1742-6596/898/4/042029). URL: <https://dx.doi.org/10.1088/1742-6596/898/4/042029> (visited on 02/27/2024).
- [30] S. Agostinelli et al. "Geant4—a simulation toolkit". *Nuclear Instruments and Methods in Physics Research Section A: Accelerators, Spectrometers, Detectors and Associated Equipment* 506.3 (July 1, 2003), 250–303. ISSN: 0168-9002. DOI: [10.1016/S0168-9002\(03\)01368-8](https://doi.org/10.1016/S0168-9002(03)01368-8). URL: <https://www.sciencedirect.com/science/article/pii/S0168900203013688> (visited on 02/27/2024).
- [31] J. Allison et al. "Geant4 developments and applications". *IEEE Transactions on Nuclear Science* 53.1 (Feb. 2006). Conference Name: IEEE Transactions on Nuclear Science, 270–278. ISSN: 1558-1578. DOI: [10.1109/TNS.2006.869826](https://doi.org/10.1109/TNS.2006.869826). URL: <https://ieeexplore.ieee.org/document/1610988?isnumber=33833&arnumber=1610988&count=33&index=7> (visited on 02/27/2024).
- [32] J. Allison et al. "Recent developments in Geant4". *Nuclear Instruments and Methods in Physics Research Section A: Accelerators, Spectrometers, Detectors and Associated Equipment* 835 (Nov. 1, 2016), 186–225. ISSN: 0168-9002. DOI: [10.1016/j.nima.2016.06.125](https://doi.org/10.1016/j.nima.2016.06.125). URL: <https://www.sciencedirect.com/science/article/pii/S0168900216306957> (visited on 02/27/2024).
- [33] Wenjie Wu, Miao He, Xiang Zhou, and Haoxue Qiao. "A new method of energy reconstruction for large spherical liquid scintillator detectors". *Journal of Instrumentation* 14.3 (Mar. 8, 2019), P03009–P03009. ISSN: 1748-0221. DOI: [10.1088/1748-0221/14/03/P03009](https://doi.org/10.1088/1748-0221/14/03/P03009). eprint: [1812.01799\[hep-ex, physics:physics\]](https://arxiv.org/abs/1812.01799). URL: <http://arxiv.org/abs/1812.01799> (visited on 07/28/2023).

- 783 [34] Guihong Huang et al. "Improving the energy uniformity for large liquid scintillator detec-  
784 tors". *Nuclear Instruments and Methods in Physics Research Section A: Accelerators, Spectrometers,*  
785 *Detectors and Associated Equipment* 1001 (June 11, 2021), 165287. ISSN: 0168-9002. DOI: [10.1016/j.nima.2021.165287](https://doi.org/10.1016/j.nima.2021.165287). URL: <https://www.sciencedirect.com/science/article/pii/S0168900221002710> (visited on 03/01/2024).
- 788 [35] Ziyuan Li et al. "Event vertex and time reconstruction in large volume liquid scintillator de-  
789 tector". *Nuclear Science and Techniques* 32.5 (May 2021), 49. ISSN: 1001-8042, 2210-3147. DOI:  
790 [10.1007/s41365-021-00885-z](https://doi.org/10.1007/s41365-021-00885-z). eprint: [2101.08901\[hep-ex, physics:physics\]](https://arxiv.org/abs/2101.08901). URL: [http://arxiv.org/abs/2101.08901](https://arxiv.org/abs/2101.08901) (visited on 07/28/2023).
- 792 [36] Gioacchino Ranucci. "An analytical approach to the evaluation of the pulse shape discrimi-  
793 nation properties of scintillators". *Nuclear Instruments and Methods in Physics Research Section*  
794 *A: Accelerators, Spectrometers, Detectors and Associated Equipment* 354.2 (Jan. 30, 1995), 389–399.  
795 ISSN: 0168-9002. DOI: [10.1016/0168-9002\(94\)00886-8](https://doi.org/10.1016/0168-9002(94)00886-8). URL: <https://www.sciencedirect.com/science/article/pii/S0168900294008868> (visited on 03/07/2024).
- 797 [37] C. Galbiati and K. McCarty. "Time and space reconstruction in optical, non-imaging, scintillator-  
798 based particle detectors". *Nuclear Instruments and Methods in Physics Research Section A: Ac-  
799 celerators, Spectrometers, Detectors and Associated Equipment* 568.2 (Dec. 1, 2006), 700–709. ISSN:  
800 0168-9002. DOI: [10.1016/j.nima.2006.07.058](https://doi.org/10.1016/j.nima.2006.07.058). URL: <https://www.sciencedirect.com/science/article/pii/S0168900206013519> (visited on 03/07/2024).
- 802 [38] M. Moszyński and B. Bengtson. "Status of timing with plastic scintillation detectors". *Nu-  
803 clear Instruments and Methods* 158 (Jan. 1, 1979), 1–31. ISSN: 0029-554X. DOI: [10.1016/S0029-554X\(79\)90170-8](https://doi.org/10.1016/S0029-554X(79)90170-8). URL: <https://www.sciencedirect.com/science/article/pii/S0029554X79901708> (visited on 03/07/2024).
- 806 [39] Gui-Hong Huang, Wei Jiang, Liang-Jian Wen, Yi-Fang Wang, and Wu-Ming Luo. "Data-driven  
807 simultaneous vertex and energy reconstruction for large liquid scintillator detectors". *Nuclear*  
808 *Science and Techniques* 34.6 (June 17, 2023), 83. ISSN: 2210-3147. DOI: [10.1007/s41365-023-01240-0](https://doi.org/10.1007/s41365-023-01240-0). URL: <https://doi.org/10.1007/s41365-023-01240-0> (visited on 08/17/2023).
- 810 [40] Zhen Qian et al. "Vertex and Energy Reconstruction in JUNO with Machine Learning Meth-  
811 ods". *Nuclear Instruments and Methods in Physics Research Section A: Accelerators, Spectrometers,*  
812 *Detectors and Associated Equipment* 1010 (Sept. 2021), 165527. ISSN: 01689002. DOI: [10.1016/j.nima.2021.165527](https://doi.org/10.1016/j.nima.2021.165527). eprint: [2101.04839\[hep-ex, physics:physics\]](https://arxiv.org/abs/2101.04839). URL: [http://arxiv.org/abs/2101.04839](https://arxiv.org/abs/2101.04839) (visited on 07/24/2023).
- 815 [41] Arsenii Gavrikov, Yury Malyshkin, and Fedor Ratnikov. "Energy reconstruction for large liq-  
816 uid scintillator detectors with machine learning techniques: aggregated features approach".  
817 *The European Physical Journal C* 82.11 (Nov. 14, 2022), 1021. ISSN: 1434-6052. DOI: [10.1140/epjc/s10052-022-11004-6](https://doi.org/10.1140/epjc/s10052-022-11004-6). eprint: [2206.09040\[physics\]](https://arxiv.org/abs/2206.09040). URL: [http://arxiv.org/abs/2206.09040](https://arxiv.org/abs/2206.09040) (visited on 07/24/2023).
- 820 [42] R. Abbasi et al. "Graph Neural Networks for low-energy event classification & reconstruction  
821 in IceCube". *Journal of Instrumentation* 17.11 (Nov. 2022). Publisher: IOP Publishing, P11003.  
822 ISSN: 1748-0221. DOI: [10.1088/1748-0221/17/11/P11003](https://doi.org/10.1088/1748-0221/17/11/P11003). URL: <https://dx.doi.org/10.1088/1748-0221/17/11/P11003> (visited on 04/04/2024).
- 824 [43] S. Reck, D. Guderian, G. Vermarien, A. Domi, and on behalf of the KM3NeT collaboration  
825 on behalf of the. "Graph neural networks for reconstruction and classification in KM3NeT".  
826 *Journal of Instrumentation* 16.10 (Oct. 2021). Publisher: IOP Publishing, C10011. ISSN: 1748-0221.  
827 DOI: [10.1088/1748-0221/16/10/C10011](https://doi.org/10.1088/1748-0221/16/10/C10011). URL: <https://dx.doi.org/10.1088/1748-0221/16/10/C10011> (visited on 04/04/2024).
- 829 [44] The IceCube collaboration et al. "A convolutional neural network based cascade reconstruction  
830 for the IceCube Neutrino Observatory". *Journal of Instrumentation* 16.7 (July 2021). Publisher:  
831 IOP Publishing, P07041. ISSN: 1748-0221. DOI: [10.1088/1748-0221/16/07/P07041](https://doi.org/10.1088/1748-0221/16/07/P07041). URL:  
832 <https://dx.doi.org/10.1088/1748-0221/16/07/P07041> (visited on 04/04/2024).

- 833 [45] DUNE Collaboration et al. “Neutrino interaction classification with a convolutional neural  
834 network in the DUNE far detector”. *Physical Review D* 102.9 (Nov. 9, 2020). Publisher: American  
835 Physical Society, 092003. DOI: [10.1103/PhysRevD.102.092003](https://doi.org/10.1103/PhysRevD.102.092003). URL: [https://link.aps.org/](https://link.aps.org/doi/10.1103/PhysRevD.102.092003)  
836 [doi/10.1103/PhysRevD.102.092003](https://doi.org/10.1103/PhysRevD.102.092003) (visited on 04/04/2024).
- 837 [46] K. M. Górski, E. Hivon, A. J. Banday, B. D. Wandelt, F. K. Hansen, M. Reinecke, and M. Bartel-  
838 mann. “HEALPix: A Framework for High-Resolution Discretization and Fast Analysis of Data  
839 Distributed on the Sphere”. *The Astrophysical Journal* 622 (Apr. 1, 2005). ADS Bibcode: 2005ApJ...622..759G,  
840 759–771. ISSN: 0004-637X. DOI: [10.1086/427976](https://doi.org/10.1086/427976). URL: <https://ui.adsabs.harvard.edu/abs/2005ApJ...622..759G> (visited on 04/04/2024).
- 841 [47] Michaël Defferrard, Xavier Bresson, and Pierre Vandergheynst. *Convolutional Neural Networks  
842 on Graphs with Fast Localized Spectral Filtering*. Feb. 5, 2017. DOI: [10.48550/arXiv.1606.09375](https://doi.org/10.48550/arXiv.1606.09375).  
843 eprint: [1606.09375\[cs, stat\]](https://arxiv.org/abs/1606.09375). URL: [http://arxiv.org/abs/1606.09375](https://arxiv.org/abs/1606.09375) (visited on  
844 04/04/2024).
- 845